



POLITECNICO MILANO 1863

SCHOOL OF INDUSTRIAL AND INFORMATION ENGINEERING
MASTER OF SCIENCE IN NUCLEAR ENGINEERING

Thermo-Mechanical Characterization of Oxide Coatings

Supervisor: Prof. Marco BEGHI
Co-supervisors: Dr. Fabio DI FONZO
Matteo VANAZZI

Author:
Essam SERAG
Matr. 874873

Academic Year 2017 - 2018

إلى والدتي الغالية وأبي العزيز

Table of Contents

Abstract	I
Abstract	III
List of Figures	V
List of Tables	VIII
1. Introduction	1
1.1 Surface Engineering	2
1.2 Surfacing Materials and Processes	2
1.3 Material/Process Selection	3
1.4 Nuclear Physics	5
1.5 Nuclear Reactions	5
1.6 Fission reactors	7
1.7 Thermal Reactors	8
1.8 Fast Neutron Reactors.....	8
1.9 Aim and Structure of The Thesis	9
2. Material Selection	12
2.1 Wear and Corrosion.....	13
2.2 Material Selection for Wear and Corrosion Resistances	14
2.3 State of The Art.....	15
a) Tungsten Oxide (W ₂ O ₃).....	15
b) Yttrium Oxide (Y ₂ O ₃)	17
c) Aluminum Oxide (Al ₂ O ₃).....	18
2.4 Comparison Between Al ₂ O ₃ & Y ₂ O ₃	19
3. Deposition Technique & Experimental Setups	22
3.1 Pulsed Laser Deposition.....	23
3.2 Brillouin Spectroscopy.....	24
3.3 Substrate Curvature Setup.....	29
3.4 Samples Preparation.....	32
4. Thermo-Mechanical Assessment of Al₂O₃ Coatings	34
4.1 Residual Stresses.....	35
4.2 Elastic Moduli	37
4.3 Coefficient of Thermal Expansion	45
4.4 Elastic Moduli for Annealed Al ₂ O ₃	49

4.5 Scattered Data on Y2O3	55
a) Residual Stress.....	55
b) Brillouin Measurement	56
c) Behavior of Yttria Under Thermal Loads.....	56
5. Conclusions & Perspectives	60
5.1 Conclusions.....	61
5.2 Perspectives.....	62
Acknowledgments.....	65
References	67

Abstract

The development and the evolution of nowadays technologies depend mainly on developing and constructing new materials that can withstand the different scenarios of a specific application.

In this work, lead-cooled fast-neutron fission reactors are taken as the application to be considered, since this type of reactors is considered a better solution for several drawbacks that face the current thermal reactors in use, such as, low Burnup, high-level radioactivity of nuclear wastes, etc.

Because of the severe conditions in the core of such reactors, like irradiation, wear and corrosion, there will be some problems which may face this technology which are strictly related to the in-core structural materials, namely, the cladding. The cladding serves as a barrier for radioactive materials which form inside the fuel pellets after a fission event, preventing them from leaking to the coolant, the cladding also serves as a component to keep the integrity of the fuel pins. As a solution for these phenomena, coatings have been introduced to protect the in-core materials, especially ceramic coatings, for their superior mechanical and thermal properties and their chemical inertness.

In this study, aluminum oxide (alumina), Al_2O_3 , has been chosen as a promising candidate ceramic to be applied as a coating for the protection of cladding material. It has been investigated intensely in the past and showed amazing behavior under thermal loads and in the erosive environment of lead. Pulsed Laser deposition technique has been used to deposit the alumina coatings on silicon substrates in order to study their thermo-mechanical properties. The elastic moduli of these coatings have been acquired using Brillouin Spectroscopy which is a non-destructive investigating technique by utilizing laser. The coefficient of thermal expansion of the investigated alumina has been measured using a relatively new experimental setup called the substrate curvature setup. The residual stresses arising within the as-deposit Al_2O_3 coatings have been studied as well, using the same setup. Furthermore, annealed Al_2O_3 samples at around $750\text{ }^\circ\text{C}$ for 20 minutes, have been investigated using, again, Brillouin Spectroscopy to get their elastic moduli.

At the beginning of this thesis work, yttrium oxide (yttria), Y_2O_3 , was chosen as a promising protective coating for the fusion reactor application, but knowing, after doing some characterization, that it does crystallize, and thus, losing the appealing properties of the amorphous phase, it has been decided to switch to Al_2O_3 . Nevertheless, some scattered data on Y_2O_3 are presented in this thesis work that may be interesting.

It is worth noting that thermo-mechanical properties of the different samples are highly dependent on the micro-structure, morphology and composition of the films which, themselves, are dependent on the deposition technique and the parameters chosen in each technique.

At the end of this thesis work, it is expected to get a full information of the just mentioned features which will, hopefully, help us to push the current frontier of this field a bit further.

Sinossi

Lo sviluppo e l'evoluzione delle tecnologie odierne dipendono principalmente dallo sviluppo e dalla costruzione di nuovi materiali in grado di resistere ai diversi scenari di un'applicazione specifica.

In questo lavoro, i reattori a fissione a neutroni veloci raffreddati a piombo sono presi come l'applicazione da considerare, poiché questo tipo di reattori è considerato una soluzione migliore per diversi inconvenienti che affrontano i reattori termici attuali in uso, come, Burnup basso, alto - attività radioattiva di rifiuti nucleari, ecc.

A causa delle gravi condizioni nel nucleo di tali reattori, come l'irradiazione, l'usura e la corrosione, ci saranno alcuni problemi che potrebbero incontrare questa tecnologia che sono strettamente correlati ai materiali strutturali interni, vale a dire il rivestimento. Il rivestimento funge da barriera per i materiali radioattivi che si formano all'interno delle pastiglie di combustibile dopo un evento di fissione, impedendo loro di fuoriuscire dal liquido di raffreddamento, il rivestimento funge anche da componente per mantenere l'integrità dei perni del combustibile. Come soluzione per questi fenomeni, sono stati introdotti rivestimenti per proteggere i materiali interni, in particolare i rivestimenti ceramici, per le loro superiori proprietà meccaniche e termiche e la loro inerzia chimica.

In questo studio, l'ossido di alluminio (allumina), Al_2O_3 , è stato scelto come candidato ceramico promettente da applicare come rivestimento per la protezione del materiale di rivestimento. È stato studiato intensamente in passato e ha mostrato un comportamento sorprendente sotto carichi termici e nell'ambiente erosivo del piombo. La tecnica di deposizione a laser pulsato è stata utilizzata per depositare i rivestimenti di allumina su substrati di silicio per studiarne le proprietà termomeccaniche. I moduli elastici di questi rivestimenti sono stati acquisiti utilizzando la spettroscopia di Brillouin che è una tecnica di indagine non distruttiva utilizzando il laser. Il coefficiente di espansione termica dell'allumina studiata è stato misurato utilizzando una configurazione sperimentale relativamente nuova chiamata impostazione della curvatura del substrato. Anche le sollecitazioni residue derivanti dai rivestimenti Al_2O_3 as-deposit sono state studiate utilizzando la stessa configurazione. Inoltre, campioni di Al_2O_3 ricotti a circa $750\text{ }^\circ\text{C}$ per 20 minuti, sono stati studiati utilizzando, ancora una volta, la spettroscopia di Brillouin per ottenere i loro moduli elastici.

All'inizio di questo lavoro di tesi, l'ossido di ittrio (yttria), Y_2O_3 , è stato scelto come rivestimento protettivo promettente per l'applicazione del reattore a fusione, ma sapendo, dopo aver effettuato una caratterizzazione, che cristallizza, e quindi perdendo le proprietà accattivanti di la fase amorfa, è stato deciso di passare ad Al_2O_3 . Tuttavia, alcuni dati sparsi su Y_2O_3 sono presentati in questo lavoro di tesi che potrebbe essere interessante.

Alla fine di questo lavoro di tesi, ci si aspetta di avere una completa informazione delle caratteristiche appena menzionate che, si spera, ci aiuteranno a spingere un po' più oltre l'attuale frontiera di questo campo.

List of Figures

Fig. 1.1- The selection process (HAZ = heat affected zone).....	4
Fig. 1.2- Fission process of U235.....	6
Fig. 1.3- Fusion process producing helium and highly energetic neutron.....	6
Fig. 1.4- An induced gamma ray emission through an incident neutron.....	6
Fig. 1.5- Schematic representation of nuclear spallation process.....	7
Fig. 2.1- Mechanisms of abrasive wear.....	13
Fig. 2.2- Mechanism of adhesive wear.....	13
Fig. 2.3- Mechanism of contact fatigue.....	14
Fig. 2.4- Physical sputtering yield for different materials bombarded with deuterium.....	16
Fig. 2.5- Inventory of tritium for different materials after different plasma discharges.....	17
Fig. 3.1- Schematic view of pulsed laser deposition setup.....	23
Fig. 3.2- Picture of Brillouin Spectroscopy.....	24
Fig. 3.3- Schematic view of Brillouin spectroscopy.....	25
Fig. 3.4- Schematic view showing Fabry-Perot interferometers.....	25
Fig. 3.5- Brillouin spectrum of metallic tungsten film.....	26
Fig. 3.6- Experimental and computed dispersion relation of a W film.....	27
Fig. 3.7- Iso-level curves for the LS estimator; the bold black lines are curves corresponding to the 68%, 90% and 95% confidence regions.....	28
Fig. 3.8- Picture of curvature substrate experimental setup.....	29
Fig. 3.9- Schematic view of the substrate curvature setup.....	30
Fig. 3.10: a) Schematic representation of two initially parallel laser beams that are reflected by a curved surface. b) The reflected beams are collected by the collecting objective and recorded by the CMOS.....	30
Fig. 4.1: a) Compressive stress within the film. b) Tensile stress within the film.....	35
Fig. 4.2- Compressive stress arises within the coating as a result of the substrate bending.....	36
Fig. 4.3- Plot of residual stress with film thickness.....	36
Fig. 4.4- Plot showing the change from compressive to tensile residual stress with respect to film thickness.....	37
Fig. 4.5- The least square map for the 250 nm sample.....	38
Fig. 4.6- The least square map for the 500 nm sample.....	39
Fig. 4.7- The least square map for the 1 μm sample.....	39
Fig. 4.8- The least square map for the 2 μm sample.....	40

Fig. 4.9- Frequency spectra for the 1 μm and 2 μm samples.....	41
Fig. 4.10- Computed dispersion curves for the 500 nm sample	42
Fig. 4.11- The two experimental points for the 500 nm sample at 50°	42
Fig. 4.12- Plot of Young's modulus of as-deposit samples with thickness.....	45
Fig. 4.13- The change of residual stress of the 250 nm sample with temperature.	46
Fig. 4.14- The change of residual stress of the 500 nm sample with temperature.	47
Fig. 4.15- The change of residual stress of the 1 μm sample with temperature.....	47
Fig. 4.16- The change of residual stress of the 2 μm sample with temperature.....	48
Fig. 4.17- Plot of coefficient of thermal expansion with thickness.	49
Fig. 4.18- XRD for 500 nm sample annealed at different temperatures for 12 h.....	50
Fig. 4.19- XRD for 1 μm sample annealed at different temperatures for 12 h.	50
Fig. 4.20- XRD for 2 μm annealed at different temperatures for 12 h.....	51
Fig. 4.21- XRD for 1 μm sample annealed at 750 °C for 45 minutes	52
Fig. 4.22- XRD for 2 μm sample annealed at 750 °C for 30 minutes.	52
Fig 4.23- Frequency spectra of 2 μm and 1 μm annealed samples.....	53
Fig. 4.24- Plot of Young's moduli of as-deposit and annealed 2 μm and 1 μm samples	54
Fig. 4.25- Residual stress within Y2O3 thin films at different thicknesses.	55
Fig. 4.26- Frequency spectrum of 1 μm yttrium oxide coating.....	56
Fig. 4.27- Evolution of residual stress within yttria 1 μm film under temperature variation.....	57
Fig. 4.28- XRD patterns for yttria film under different annealing temperature	58

List of Tables

Table 1.1- Comparison of surface processes and deposits	4
Table 4.1- Mass density ρ , Young's modulus E , Poisson ratio ν , bulk modulus B and shear modulus G of sapphire	43
Table 4.2- Young's modulus E , Poisson ratio ν , bulk modulus B , shear modulus G and elastic constants (C_{11} , C_{44}) values of the 250 nm sample	43
Table 4.3- Young's modulus E , Poisson ratio ν , bulk modulus B , shear modulus G and elastic constants (C_{11} , C_{44}) values of the 500 nm sample.....	44
Table 4.4- Young's modulus E , Poisson ratio ν , bulk modulus B , shear modulus G and elastic constants (C_{11} , C_{44}) values of the 1 μm sample	44
Table 4.5- Young's modulus E , Poisson ratio ν , bulk modulus B , shear modulus G and elastic constants (C_{11} , C_{44}) values of the 2 μm sample	44
Table 4.6- Young's modulus E , Poisson ratio ν , bulk modulus B , shear modulus G and elastic constants (C_{11} , C_{44}) values of the 1 μm annealed sample	53
Table 4.7- Young's modulus E , Poisson ratio ν , bulk modulus B , shear modulus G and elastic constants (C_{11} , C_{44}) values of the 2 μm annealed sample	54

1. Introduction

Throughout this chapter an introduction of surface engineering and the importance of coatings, in nowadays applications in different fields, is given, furthermore, the material/process selection method in addition to the various processes used to deposit coatings will be briefly mentioned.

A brief introduction of nuclear physics and its principles with its two-folding nature, fission and fusion, will also be stated, a comparison between thermal and fast reactors is also provided. Last but not least, the aim and frame of this thesis work will be defined.

1.1 Surface Engineering

Wear and corrosion lead to deterioration of metallic surfaces in use, which leads to loss of efficiency of the operating system, or even worse, a breakdown. Wear and corrosion in equipment cost industry a lot, realizing this fact is the reason behind the development of the “surface engineering” technology. Surface engineering includes the application of coatings to metallic surfaces to improve their performance. This is a subject of great importance to industry, which relies on long, trouble-free operation of plant to obtain uniform product quality and lowest possible product cost.

The requirements of the material to provide the component in use with the required strength are different from those which provide the component with wear and corrosion resistance, so a product consisting of structural material with a protective layer on the surface is the most appropriate solution which comes to mind.

There are several uses of surfacing other than preventing wear and corrosion which are also of great economic importance. Electrically resisting or conducting layers and layers which act as thermal barriers between the equipment and its working environment are also introduced by surface technology.

1.2 Surfacing Materials and Processes

Most metals, alloys, ceramics and some intermetallic compounds can be applied as coatings either individually or as mixtures, but their characteristics often limit the processes that can be used for their application.

The material/process relationship identifies when they can be used together, furthermore, it determines the properties that can be expected from the coating, such as density and adhesion to the substrate.

Processes:

❖ Welding

The highest bond strength achieved between deposit and substrate is provided by welding process. With few exceptions, deposits of considerable thickness can also be applied with this process. It can be operated both manually or be automatized and programmed.

❖ Thermal spraying

Thermal spraying offers two significant advantages over weld surfacing. The first is that both non-weldable coating materials, such as ceramics, can be deposited as well as materials which are also weldable. The second is that all these materials can be deposited on substrate materials that are unsuited to welding either because of their composition or because their thin section would distort excessively when welded.

Compared with welded coatings, thermally sprayed deposits exhibit some porosity and a lower bond strength to the substrate. In general, deposit thickness is less than is possible by welding. Provided that these factors are taken into account at the design stage, thermal spraying can, and does, provide excellent and reliable service in applications as demanding as aircraft gas turbine engines.

❖ Electrodeposition

Electrodeposition offers a more limited range of coating materials, but the low temperature of deposition provides advantages of low distortion, better access to internal surfaces and accurate control of deposit thickness.

❖ Vapor deposition

Vapor deposition provides a limited range of coating material possibilities but can be used with materials that are difficult or impossible to apply by other techniques, or to produce thin coatings of controlled thickness. The ranges of thickness that are possible for each process are given in table 1.1 [87].

1.3 Material/Process Selection

Selection of material and process may seem difficult under the wide range of the possibilities, but basically it is straightforward. Often there are constraints placed on the choice because of availability. In many cases there is a precedent, but when considering a new problem, it helps to follow a checklist of the type shown in figure 1.1 [87].

There is a sequence of several decisions to be made which covers fundamental points. The first is to be aware and clear about the service conditions, either by experience or plant design data. This is the key to material selection. The second decision is related to the choice of process to implement that material, which will involve questions of compatibility between the process and the material. As may be known, not all the materials can be applied by all processes. A further question of compatibility arises between both material and process with the substrate. All these questions should be considered to resolve the material/process selection matter.

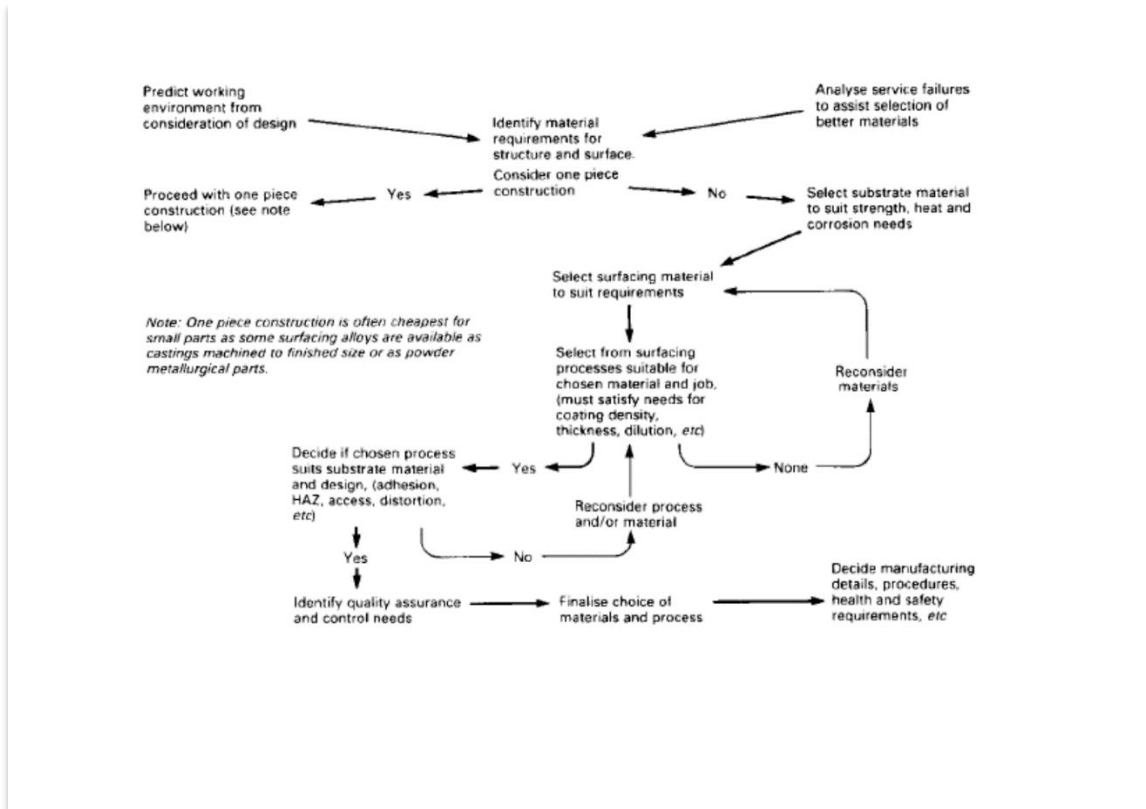


Fig. 1.1- The selection process (HAZ = heat affected zone).

Table 1.1- Comparison of surface processes and deposits.

	Vapour deposition	Electrodeposition	Thermal spraying	Spray fusing	Welding
Thickness/mm	0.001-0.2	0.02-0.5	0.1-1.0	0.5-1.5	1-20 or more
Component geometry	Versatile	Versatile	Access to internal surfaces controlled by size of torch/gun		
Component size	Limited by chamber size	Limited by plating bath	No limit	Limited by fusing facility	No limit
Substrate material	Almost limitless	Almost limitless	Almost limitless	Metals or alloys of higher melting point than coating	
Substrate temperature/°C	30-1000	100	200	1050	1400
Pretreatment	PVD - ion bombardment CVD - various	Chemical cleaning and etching	Clean and roughen surface		Mechanical cleaning
Post-treatment	None/stress relief	None/stress relief	None	Substrate anneal/stress relief as required	
Coating porosity/%	Nil to small	Nil to small	1-15	Nil	Nil
Bond strength/MPa	High	100	20-140	High	High
Bond mechanism	Atomic, surface forces	Surface forces	Mechanical	Metallurgical	Metallurgical
Control of deposit thickness	Good	Good	Fairly good	Moderate	Manual - variable Mechanised - good
Distortion of substrate	Low	Low	Low	Moderate	Can be high, depending on substrate geometry

PVD = physical chemical deposition, CVD = chemical vapour deposition.

1.4 Nuclear Physics

After discussing the general concepts of surface engineering and stating the different coating deposition processes, and since protecting structural materials of nuclear installations has been chosen as an application for these protective coatings, it is time to move to the definition of the nuclear physics and why it is extremely important to study this field.

Nuclear physics is a field of science that studies atomic nuclei, their constituents and interactions. Discoveries in nuclear physics have led to applications in many fields. This includes nuclear power, nuclear medicine, ion implantation in materials engineering, radiation dating in geology and archeology, and unfortunately, nuclear weapons.

Heading now to the different types of nuclear reactions and concentrating on fission reaction and the type of reactors based on it, especially fast fission reactors for their appealing advantages over thermal reactors.

1.5 Nuclear Reactions

Nuclear reaction is a process in which two nuclei, or else a nucleus of an atom and a sub-atomic particle from outside the atom, collide to produce one or more nuclides that are different from the nuclide(s) that began the process.

In principle, more than two particles colliding may collide in a reaction, but because the probability of three or more nuclei to meet at the same time at the same place is much less than for two nuclei, such an event is exceptionally rare.

Types of Nuclear Reactions:

While the number of possible nuclear reactions is immense, there are several types which are more common, or otherwise notable, see figures 1.2, 1.3, 1.4 and 1.5. Some examples include:

- Fusion reactions is a process where two light nuclei join to form a heavier one.
- Fission reactions is a process where a very heavy nucleus splits into two or sometimes three pieces, after absorbing additional light particles (mainly neutrons).
- Spallation is considered when a nucleus is hit by a particle with sufficient energy and momentum to knock out several small fragments or smash it into many fragments.
- Induced gamma emission belongs to a class in which only photons were involved in creating and destroying states of nuclear excitation.

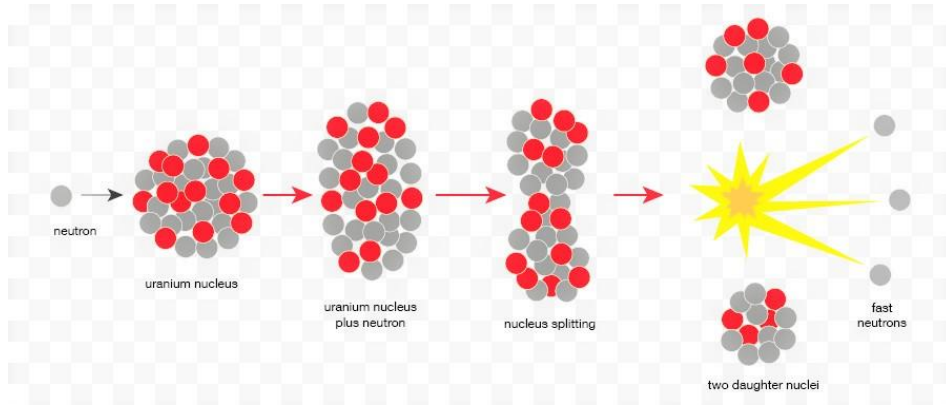


Fig. 1.2- Fission process of U235.

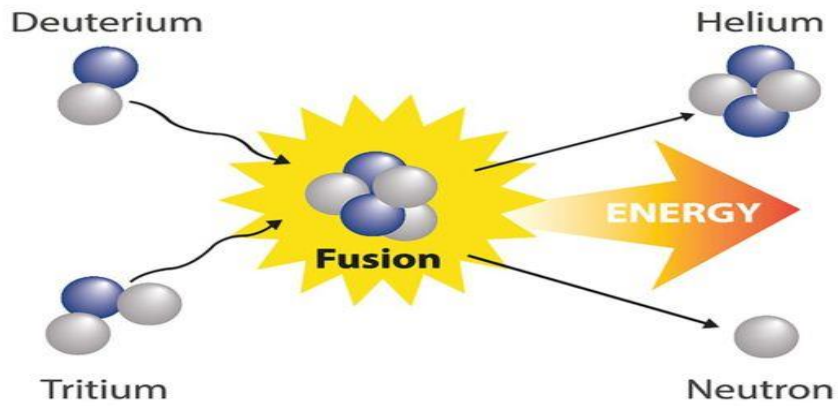


Fig. 1.3- Fusion process producing helium and highly energetic neutron.

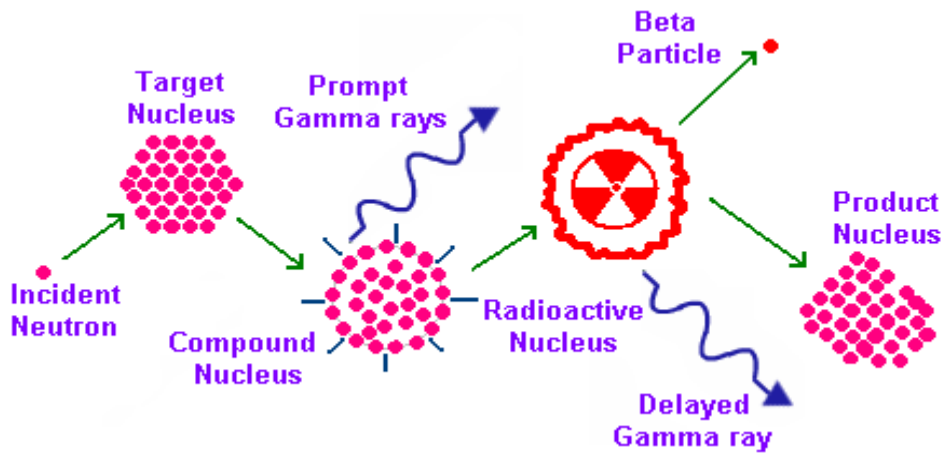


Fig. 1.4- An induced gamma ray emission through an incident neutron.

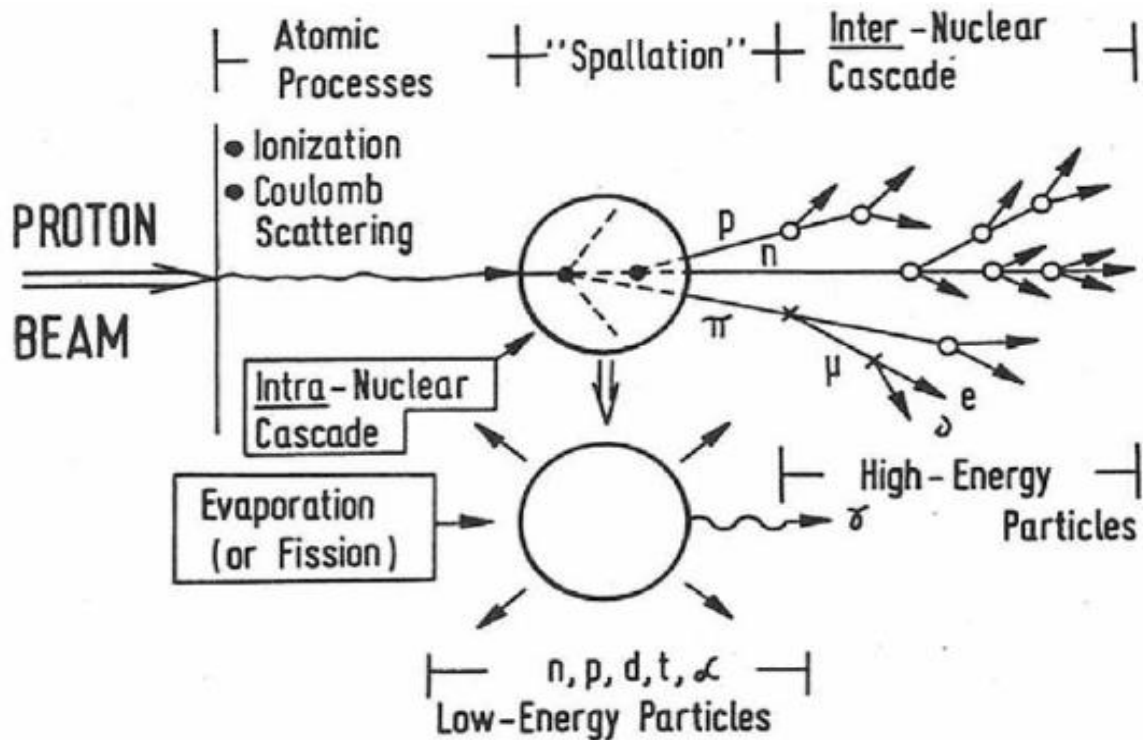


Fig. 1.5- Schematic representation of nuclear spallation process.

1.6 Fission reactors

Critical fission reactors are the most common type of nuclear reactors. In a critical fission reactor, neutrons produced by fission of fuel atoms are used to induce yet more fissions, to sustain a controllable amount of energy release. Devices that produce engineered but non-self-sustaining fission reactions are subcritical fission reactors. Such devices use radioactive decay or particle accelerators to trigger fissions.

Critical fission reactors are built for three primary purposes:

- Power reactors are intended to produce heat for nuclear power.
- Research reactors are intended to produce neutrons and activate radioactive sources for scientific, medical, engineering, or other research purposes.
- Breeder reactors are intended to produce nuclear fuels in bulk from more abundant isotopes.

While, in principle, all fission reactors can act in all three capacities, in practice the tasks lead to conflicting engineering goals and most reactors have been built with only one of the above tasks in mind.

1.7 Thermal Reactors

Thermal-neutron reactors use slow or thermal neutrons to induce fission reaction. Most nuclear power plant reactors are thermal reactors and use a neutron moderator to slow neutrons until they approach the average kinetic energy of the surrounding particles, that is, thermalize neutrons.

Thermal reactors consist of the following:

- Neutron moderator to slow down the neutrons. In light water reactors and heavy water reactors it doubles as the nuclear reactor coolant.
- Nuclear fuel, which is a fissile material, usually uranium.
- Reactor vessel that is a pressure vessel containing the coolant and reactor core.
- Radiation shielding to protect people and the environment from the harmful effects of ionizing radiation.
- Containment buildings which is designed, in any emergency, to contain the escape of radiation.
- Instrumentation to monitor and control the reactor's systems.

1.8 Fast-neutron Reactors

Fast-neutron reactors (FNR) or simply, fast reactors are a category of nuclear reactors in which the fission chain reaction is sustained by fast neutrons, as opposed to thermal neutrons used in thermal-neutron reactors. Such a reactor needs no neutron moderator, but requires fuel that is relatively rich in fissile material when compared to that required for a thermal-neutron reactor to compensate the low fission cross section of the fast neutrons to fissile materials.

Fast reactors consist of the same components as thermal ones except that the coolant is not water because it is not feasible since it works as a moderator, however, one of generation IV reactors is supercritical water reactor with decreased water density to ensure a hard-enough neutron spectrum to be considered as fast reactor [88].

Advantages over thermal-neutron reactors

- FNRs can reduce the total radiotoxicity of nuclear waste, and its lifetime. They can use all or almost all of the fuel in the waste.
- Fast reactors technically solve the "fuel shortage" argument against uranium-fueled reactors, they permit nuclear fuels to be bred from almost all the actinides. On average, more neutrons per fission are produced by fast neutrons than from **thermal neutrons**. This results in a larger surplus of neutrons beyond those required to sustain the chain reaction which means that fast reactors have the ability to breed more fuel than they consume. Such designs are known as **fast breeder reactors**.

Disadvantages

- The main disadvantage of fast-neutron reactors is that they are costly to build and operate and are not likely to be cost-competitive with thermal-neutron reactors unless the price of uranium increases dramatically.
- Due to the low cross sections of most materials at high neutron energies, higher enrichment should be provided in fast reactors which means much higher critical mass is in a fast reactor than in a thermal reactor.

Of course, these drawbacks can be tolerated when considering the much better merits provided by this type of reactors.

All operating fast reactors are molten metal cooled fast reactors, mainly using molten lead or molten sodium. New concept of coolant is to use molten salt in which salt moderating properties are insignificant.

Gas-cooled fast reactors have been the subject of research commonly using helium, which has small absorption and scattering cross sections, thus preserving the fast neutron spectrum without significant neutron absorption in the coolant.

Molten lead has been used as a coolant for its excellent neutron properties (low absorption) and its good properties as gamma ray shielding, also its high boiling point plays a crucial role of choosing it. Its high melting point is considered as a drawback since it becomes trickier to reload the core of the reactor with new fuel rods. For these reasons, molten lead fast reactors have been chosen in this work to be the type of reactors to be protected using coatings.

However, the development of lead fast reactors is directly linked to the ability to find suitable materials for the most demanding conditions. The greatest challenges arise from the extremely corrosive environment and the intense radiation fields to which materials will be exposed during operation [86]. Those issues will affect in-core components, especially fuel cladding, for which the anticipated operating temperatures and the radiation damage exposures are the highest.

1.9 Aim and Structure of The Thesis

Reaching the final part of the introductory chapter, the aim and the structure of this work are to be discussed here.

As previously mentioned, the main problem which faces the nuclear industry nowadays, apart from dealing with radioactive nuclear waste and whether to just dispose it or to reprocess it, is structural material protection against the severe conditions in the core of the reactor (thermal loads, irradiation, wear, corrosion, etc.).

The material limitation of nuclear reactors is far from being minor problem since it is hugely related to the economics and the feasibility of constructing a reactor in the first place. To preserve the integrity of the structural materials different types of coatings have been used and investigated in state of the art.

The aim of this thesis work is to develop and deposit ceramic coatings and then investigate thermo-mechanical properties of those coatings using novel and non-destructive techniques, comparing them with previously investigated ceramics, which already proved their effectivity, in the state of the art.

This book is consisted of five chapters in which one of them is this introductory chapter while the four remaining ones are going to be about 1) material selection 2) the deposition technique alongside the experimental setups used to investigate the material 3) thermo-mechanical assessment of Al₂O₃ coatings 5) conclusions and perspectives.

2. Material Selection

This chapter will start with the definitions and mechanisms of wear and corrosion, alongside how to control these phenomena through surface technology. One of the most important aspects when considering any kind of application is material selection.

Throughout this chapter, a justification of selecting the material used in this study will be given based on previous materials used in the state of the art, which have shown outstanding performance when it comes to the tribological and mechanical properties.

2.1 Wear and Corrosion

Wear can be defined as the progressive loss of material from the operating surface of the body, occurring as a result of relative motion of the surface with respect to another body. The concept includes metal to metal, metal to other solids and metal to fluid contact, and the definition clearly associates the process with the surfaces of materials.

The three basic wear mechanisms are generally considered to be abrasion, adhesion and contact fatigue, see figures (2.1), (2.2) and (2.3). However, more than one type of wear is encountered in almost all the situations. In addition, the product of one type of wear may cause secondary wear by another mechanism. The interdependence of these processes should be kept in mind all the time.

An intensification of the damage occurs under the presence of other processes such as corrosion. Corrosion of metals can be divided into two major categories: reactions with gases and reactions with liquids. While there is a strong chemical similarity between them, the transport mechanisms for the reacting species differ significantly.

During the last decade, many investigations have been carried out regarding the mechanisms of corrosion of steels in heavy liquid metals such as lead, lead-bismuth eutectic (LBE), and lead-lithium eutectic (LLE) [70–72]. The most important phenomena include oxidation and dissolution [73–78], flow accelerated corrosion [79], grid-to-rod fretting [80] and heavy liquid metals assisted loss of mechanical properties, such as liquid metal embrittlement and low cycle fatigue [81,82], or liquid metal assisted creep [83]. Among these, oxidation and dissolution are the most studied corrosion modes.

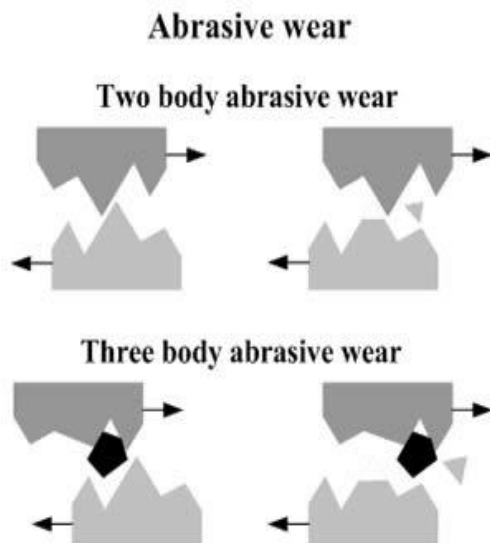


Fig. 2.1- Mechanisms of abrasive wear.

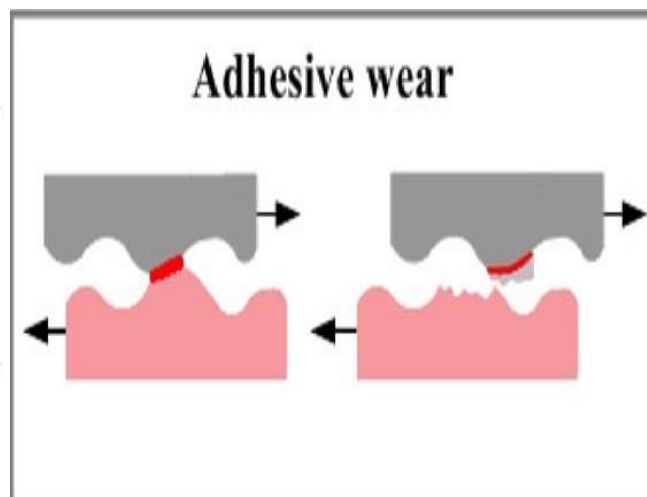


Fig. 2.2- Mechanism of adhesive wear.

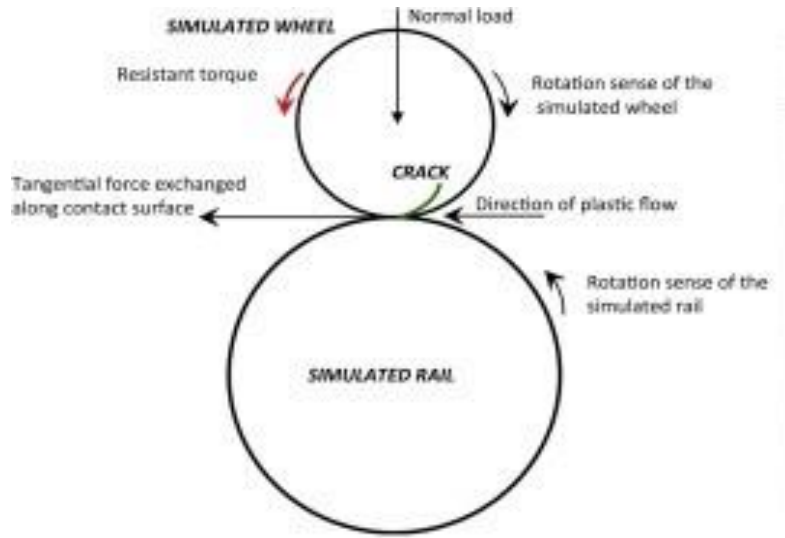


Fig. 2.3- Mechanism of contact fatigue.

2.2 Material Selection for Wear and Corrosion Resistances

The selected coating should possess good mechanical and tribological properties to overcome the harsh and severe environment in the core of lead fast reactors (wear, corrosion, irradiation, etc.), furthermore a low degree of activation should also be considered when considering any application related to the nuclear industry.

A better resistance against abrasion is guaranteed with harder surfaces. It is necessary to make sure that there is sufficient strength and toughness to resist and withstand stresses and impacts. Under large impact loadings a tougher matrix may be considered at the expense of wear-resistance, or an initially soft matrix which transforms during service. Generally, the macro-hardness of the material to resist abrasion should be at least 80% of the hardness of the abradant.

A compromise should be done between the two material requirements, strength and toughness. It should always be the extra toughness which is favored since reduced component life is less problematic than component failure.

Materials containing hard matrix with evenly distributed hard particles may be considered as a good structure for the protection against wear. The amount and size of those particles and the properties of the matrix are related to the wear conditions, which may be metal-to-metal at high or low velocity, abrasion by various particles, erosion by liquid or gas.

Regarding corrosion protection, several metals and alloys are inherently corrosion resistant such as steel alloys containing chromium to maintain a protecting chromium oxide layer on the surface. These are good choices for corrosion-resistant coatings. However, if they are cathodic to the metal underneath, they will only maintain their corrosion protection when the coating is undamaged.

Zinc and aluminum are commonly used as coatings which offer sacrificial protection to iron and mild steel in aqueous environments, and these have the advantage that damage to the coating does not lead to the immediate corrosion to the material underneath. Lead coatings are used in many applications, since lead resists attack by many chemical substances, including most acids.

Coatings derived from ceramics, such as alumina, Titania and other oxides, silicide, aluminides or polymers, offer protection owing to their inherent corrosion resistance. Most are not only corrosion-resistant themselves, but also form a physical barrier preventing access of the corroding material to the metal surface [87].

Finally, according to the different types of wear mechanisms and corrosion that materials undergo during plant operation, oxide ceramic coatings have been chosen as candidates for material protection against these phenomena because of their high hardness, their high melting points and their inherent corrosion resistance.

2.3 State of The Art

Several studies have been conducted on several ceramic materials to investigate their reliability when it comes to corrosion and irradiation resistance in both fast and fusion nuclear reactors. Some of the studies done on those ceramics will be considered, in order to build a good base for the reasons of selecting the material considered in this study.

a) Tungsten Oxide (W₂O₃)

Tungsten has been considered among other materials as a very good candidate to be used as a protective coating for the plasma facing materials (PFM). The PFMs are subjected to an extreme condition in fusion reactors, that is why choosing a proper material for the protection is crucial.

The material used to protect the PFMs has to be characterized with some features, such as, low physical and chemical sputtering yields to minimize erosion, that will lead to lower pollutants in the plasma which in turn will lead to decrease radiative power losses.

Also, a lower nuclear fuel retention is a crucial feature to eliminate as much as possible any problem concerning tritium inventory. A material with low activation yield is necessary to minimize any radiative capture events.

In order to withstand the extreme thermal loads inside the reactor, good thermomechanical properties are required, such as, high melting temperature, high thermal conductivity, high yield and ultimate strengths. Last but not least, resistance against neutrons damage is an important feature to preserve the structural integrity of the material and extend its lifespan.

As may be already known, there is no material which satisfies all these requirements, so a compromise must be done according to the design of the plant. One may work with low Z materials (e.g. carbon (C)), to minimize plasma pollution, or with high Z materials (e.g. tungsten (W), molybdenum (Mo)), ensuring a low sputtering yield.

Tungsten is a high Z metal ($Z = 74$) that shows the highest melting point among all metals (~ 3695 K), it has a good thermal conductivity (~ 174 W m $^{-1}$ K $^{-1}$), it is of particular interest for its lowest sputtering yield and fuel retention compared to the other mentioned materials, see figures 2.4 and 2.5.

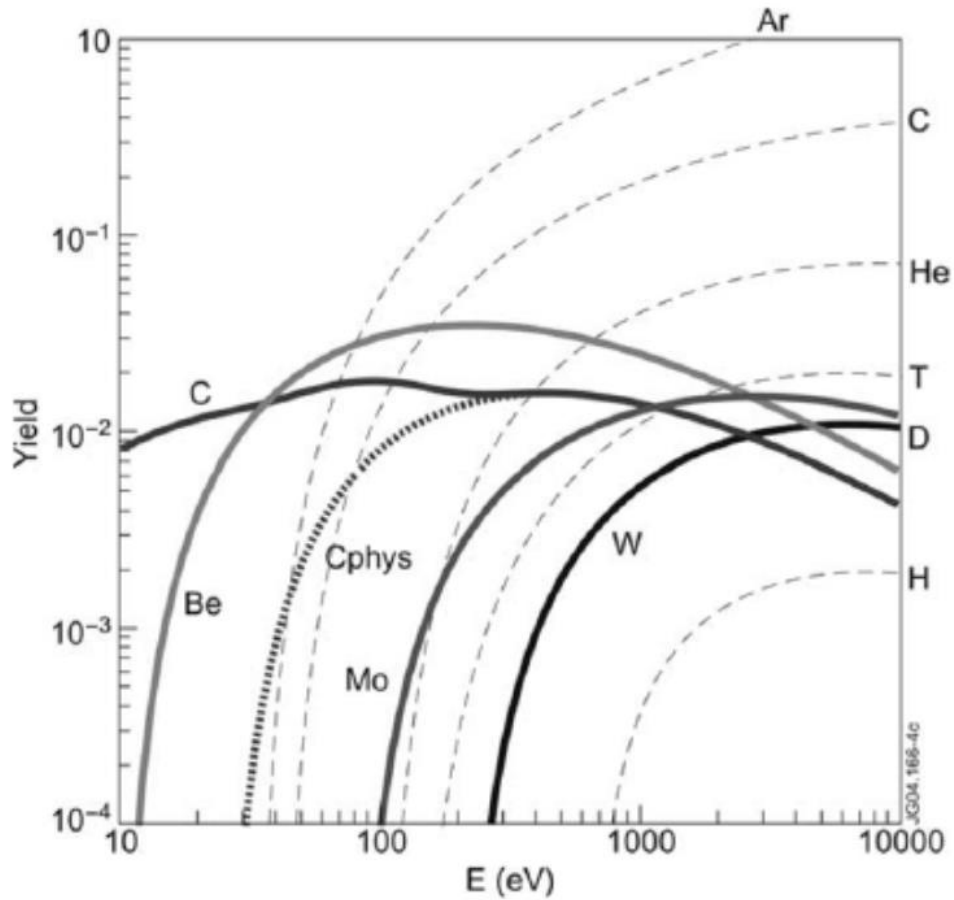


Fig. 2.4- Physical sputtering yield for different materials bombarded with deuterium. In the case of W, sputtering yield for various colliding particles are plotted with dashed lines [89].

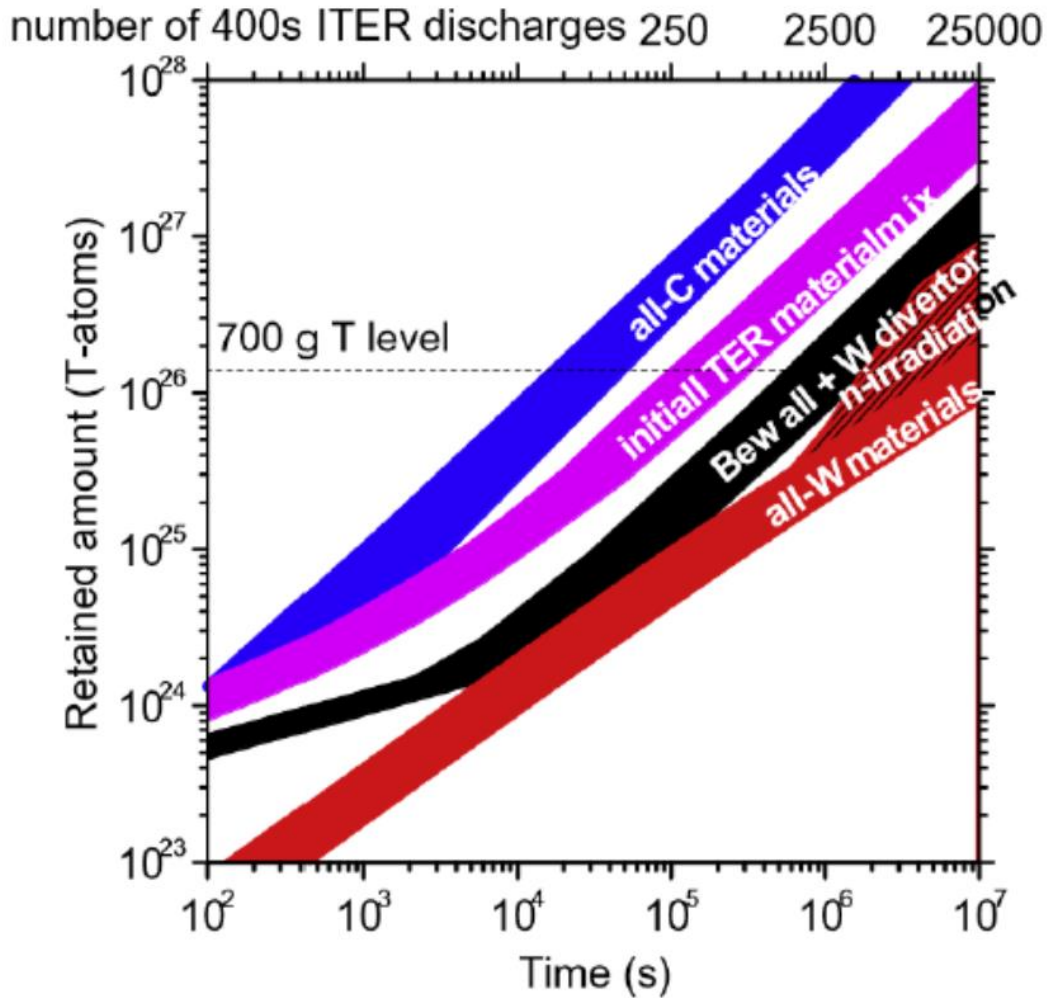


Fig. 2.5- Inventory of tritium for different materials after different plasma discharges [90].

b) Yttrium Oxide (Y₂O₃)

Yttrium oxide has been investigated during the last several years for its appealing scientific and technological applications [1–27]. Y₂O₃ has been in use in the development of functional ceramics for solid oxide fuel cells, nuclear engineering, high-temperature protective coatings, and metal-reinforced composites for high strength structural components [27–33].

Furthermore, Y₂O₃ films exhibit excellent electronic properties such as optical transparency over a broad spectral range (0.2–8 μm), high dielectric constant (14–18), high refractive index (2), large band gap (5.8 eV), low absorption (from near-UV to IR), and superior electrical break-down strength (>3 MV/cm) [1–12,18–20].

These properties make Y₂O₃ films interesting for various optical, electrical and electro-optic devices. In addition, lattice mismatch and low leakage current with silicon (Si) substrates opens several other avenues to integrate the material with Si-based devices for emerging nanotechnology [1–12].

Yttrium oxide exhibits several structural polymorphisms: C- cubic (Ia₃), B-monoclinic (C2/m), A-hexagonal (P32m), H-hexagonal (P6₃/mmc) and X-fluorite (Fm3m) [52,53]. In a series of studies by Gaboriaud et al. [55,56], it is shown that the formation of the monoclinic phase is attributed mainly to the accommodation of crystal defects like excessive oxygen vacancies.

In ambient pressure and room temperature, Y₂O₃ is a c-type rare-earth oxide [23–25]. The c-type structure is a modified fluorite-type cubic structure with one fourth of the anion sites vacant and regularly arranged [3]. This phase of Y₂O₃ is the most stable up to 2327 °C in air [23,24], at this temperature, it is transformed to H-hexagonal phase, it may also be transformed to B-monoclinic phase at ~10 GPa [51,54]. Therefore, in low temperature region (< 2327 °C), the cubic phase, as the stable phase, is normally preferred.

The growth and structural analysis of Y₂O₃ films on Si has got considerable attention due to the possibility of direct integration into electrical, optical and electro-optic devices. Choosing Si as the substrate is mainly due to the small lattice mismatch between Y₂O₃ and Si [$a(\text{Si}) \times 2 = 1.086 \text{ nm}$; $a(\text{Y}_2\text{O}_3) = 1.0604 \text{ nm}$] [1–15].

Fabrication of Y₂O₃ films can be done exploiting a wide variety of physical and chemical deposition techniques. Under physical deposition methods, molecular beam epitaxy (MBE) [34,35], electron-beam evaporation [36,37], pulsed laser deposition (PLD) [38–41], DC reactive sputtering [42,43], rf-sputtering [20–22,44,45], and ion-beam assisted deposition [4,9,13] were used to grow Y₂O₃ films. The chemical deposition methods include atomic layer deposition (ALD) [2,3,5,6], chemical vapor deposition (CVD) [46–48], metal organic chemical vapor deposition (MOCVD) [49] and reactions of inorganic and organic peroxides with metal organic complexes soluble in supercritical carbon dioxide [50].

c) Aluminum Oxide: A Promising Candidate

In recent years, significant attention was given to aluminum oxide for its possibility to be integrated into a wide range of scientific and technological applications. Bulk aluminum oxide is expected to perform in an outstanding way in applications that require hardness and resistance to wear. However, as a ceramic material, it also has some drawbacks, including brittleness and low mechanical compatibility with steels.

Since the characterization of the material is done according to its microstructure, its properties could be different from the bulk's ones. Ideally, protective barriers should attain full density and compactness, high wear resistance, good mechanical compatibility with steels and strong adhesion.

Aluminum oxide is chosen as a protective coating for several reasons, first, it shows good thermo-mechanical and phase stability under severe conditions and high temperatures. It also shows a very good chemical stability, that is why it is very hard to get aluminum from alumina, furthermore, it is highly resistant to corrosion and dissolution in the harsh environment of molten lead, also thanks to its high melting point (~ 2070 °C), it is possible to consider it in very high temperature environment. An additional reason to consider it as a protective coating in nuclear industry is its low activation yield.

Alumina exhibits a number of polymorphs [100-104], α , K, δ , θ , γ , etc. α -Al₂O₃ (corundum) is the stable phase, while all the others are metastable. Normally, amorphous phase forms at low temperatures,

γ -alumina phase becomes dominant at intermediate temperatures and K and α -Al₂O₃ phases tend to grow at higher temperatures. The formation of these phases is often dependent on the method of deposition, deposition parameters and particularly the substrate temperature.

Optical, structural and mechanical properties of PLD grown Al₂O₃ have been focused on in previous studies [63–65], alongside its application in environmental barriers [66]. These investigations have suggested that the mechanical performance of PLD grown alumina is outstanding.

Alumina is used in several technological applications ranging from hard and fully dense protective coatings to porous with high specific surface area supports for catalysis. The different coating microstructures, varying from fully dense and compact to columnar and porous can be obtained by adjusting the deposition conditions [68]. In this work, a fully dense and compact Al₂O₃ coating is grown by PLD on silicon substrates.

The deposition conditions are chosen according to the results from a previous study to obtain an advanced nanocomposite with metal-like mechanical properties, strong adhesion force and outstanding wear resistance [69]. All these features are desirable for long-term operation of the ceramic coating-alloy substrate system in heavy liquid metals at high temperature.

The crystallization temperature, electrical, optical and mechanical properties of Al₂O₃ depend highly on the surface structure, chemistry and morphology, which in turn are controlled by the deposition technique, growth conditions and post-deposition processes.

2.4 Comparison Between Al₂O₃ & Y₂O₃

At the beginning of this thesis, a preliminary study has been conducted to investigate the thermo-mechanical properties of yttria coatings as it was considered as a promising candidate material for the protection against corrosion of PbLi, in water-cooled Pb-16Li breeder concept of a fusion reactor, since PbLi solubility of the elements forming the alloy (Fe, Cr and Ni), are much higher than molten Li, leading to a higher dissolution than Li [91,92].

The experiments using XRD and the substrate curvature setups showed that yttria is not stable from thermodynamic point of view, since it tends to crystallize at very low temperatures ~ 220 °C, losing the appealing mechanical properties of the compact amorphous microstructure.

Alumina is not chemically stable in presence of Li since it forms LiAlO_2 in Pb-17Li at 800 °C, and this layer was thought as not resistant against corrosion leading to alloy dissolution. But it turned out that under iso-thermal conditions for 1000 h at 800 °C, the LiAlO_2 layer maintained the expected corrosion resistance as there was no observation of alloy dissolution [98]. However, for eutectic Pb–Li, the activity of Li is very low [93] and this allows Al_2O_3 to be considered as a protective layer in this system [94].

The singular combination of all the features, mentioned in last section and here, makes of PLD grown Al_2O_3 coatings a suitable and promising candidate for protecting steels from corrosion in heavy liquid metals at high temperatures. Thus, in this thesis work, aluminum oxide is the case study based on material, and it is deposited as a thin film exploiting the PLD technique [95].

In any case, the experiments done on yttria will also be mention in this book, even if the interest in it has been lost as it is part of this thesis work.

3. Deposition Technique & Experimental Setups

Going through this chapter, the technique which has been used to deposit the samples under certain conditions will be discussed, furthermore the different experimental setups used to investigate and asses the thermo-mechanical properties and residual stresses of the samples will be explained. Lastly, samples preparation and the conditions under which they were deposited are to be stated alongside the steps taken to measure them using the different setups.

3.1 Pulsed Laser Deposition

As already stated in the previous chapter, aluminum oxide has been chosen for our proposed application of protecting the cladding of lead-cooled fast reactors. In order to deposit this ceramic material, several deposition techniques are available such as vacuum evaporation, sputter deposition, cathodic arc deposition, etc. which are physical vapor deposition techniques (PVD). There are also some chemical vapor deposition techniques (CVD) such as plasma assisted CVD and atomic layer deposition which can also be used.

Pulsed laser deposition (PLD) is a versatile physical vapor deposition technique for deposition of thin films of a variety of materials [57]. In this method, a target, which can be in either, solid or liquid form, is evaporated using a focused high-power pulsed laser beam and the ejected species are then condensed on a substrate surface [58].

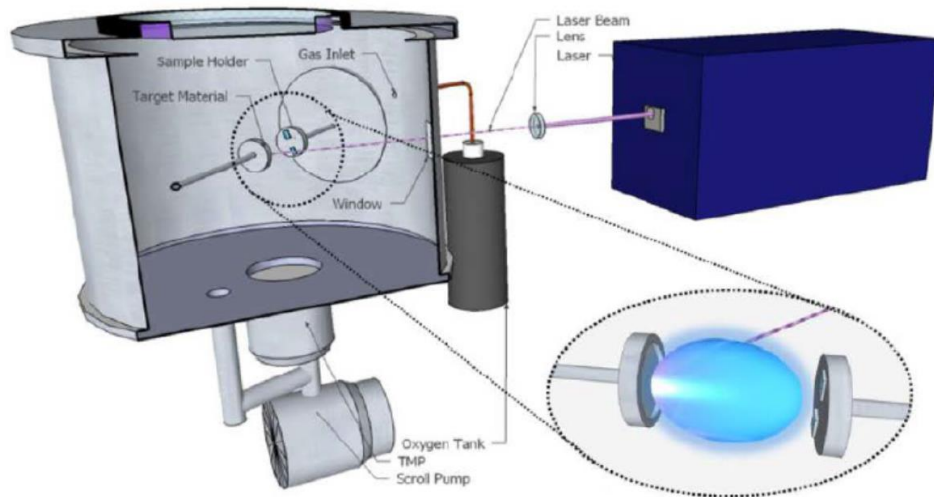


Fig. 3.1- Schematic view of pulsed laser deposition setup.

The laser-target interaction is not trivial process where the mechanism of ablation depends on the laser characteristics, as well as on the physical and mechanical properties of the target. Energy conversion process occurs when the laser radiation is absorbed by the target, where the electromagnetic energy is eventually converted into thermal and mechanical energy to cause evaporation of the target material. Evaporated material forms a plume consists of energetic (kinetic energy) particles, see figure 3.1, where eventually they hit the Si substrate and forms thin films. The deposited films possess a Gaussian thickness profile.

PLD technique has several advantages, namely, high reproducibility, accurate stoichiometry, purity in relation to the crystalline structure and phase of the deposited film, along with good control over deposition rate [59,60]. In addition of being an environment friendly process, PLD has also the possibility to operate with a high degree of automation requiring minimum human intervention, avoiding handling of corrosive and hazardous chemicals often employed in other conventional coating or deposition techniques [61]. PLD is suitable compared to other techniques for deposition of complex oxide films, since it preserves stoichiometry of deposited film through removal of all elements of the oxide target with almost equal ease [40].

However, PLD technique faces some limitations, such as, scaling up of the process for large area deposition with high deposition rates. The presence of macroscopic particulates in the deposited film and the inhomogeneous nature of the plume represents another drawback associated with PLD. Several techniques have been developed to minimize the density of macroscopic particulates presented in the deposited film [57,61]. It has been demonstrated using PLD systems designed for large area coating, the ability to deposit thin films on substrates having diameter 200 mm, despite the narrow angular width of the ablated plume [57,62].

3.2 Brillouin Spectroscopy

Brillouin spectroscopy is a well-established technique in investigating the mechanical properties of both bulk and surface materials, see figure 3.2. Mechanical properties of coatings may differ from the ones corresponding to the bulk form as previously stated in the second chapter, affected by the structure, morphology and composition.

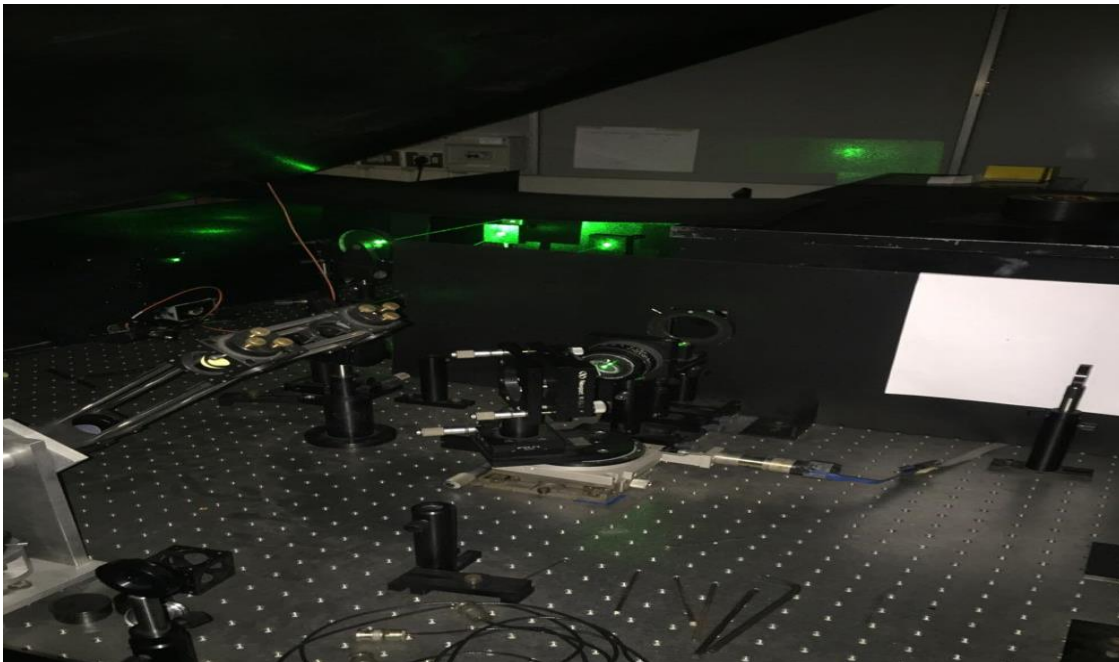


Fig. 3.2- Picture of Brillouin Spectroscopy.

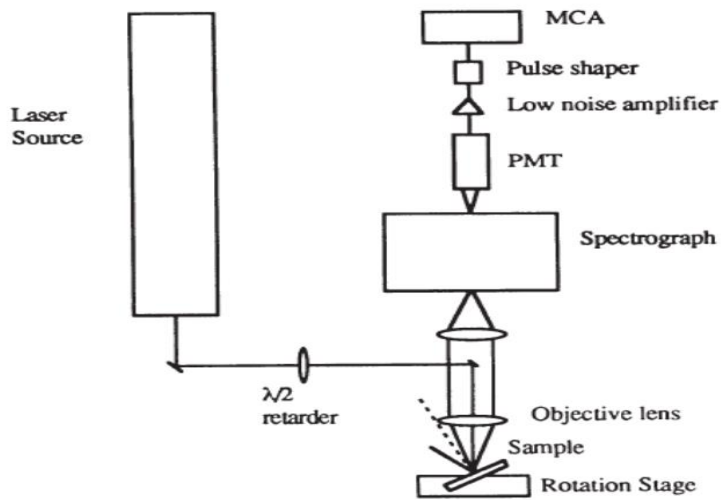


Fig. 3.3- Schematic view of Brillouin spectroscopy.

Brillouin spectroscopy is a non-destructive technique in which a laser is incident on the sample surface interacting (scattering interaction) with thermally excited elastic waves in the material (phonons). When laser is scattered inelastically, its frequency either increases or decreases depending on two different events, annihilation or creation of phonons, respectively.

The scattered laser is then focused and passes through a set of Fabry-Perot interferometers of the Sandercock type, see figures (3.3) and (3.4), reaching eventually to a photomultiplier allowing us to acquire a frequency spectrum [96].

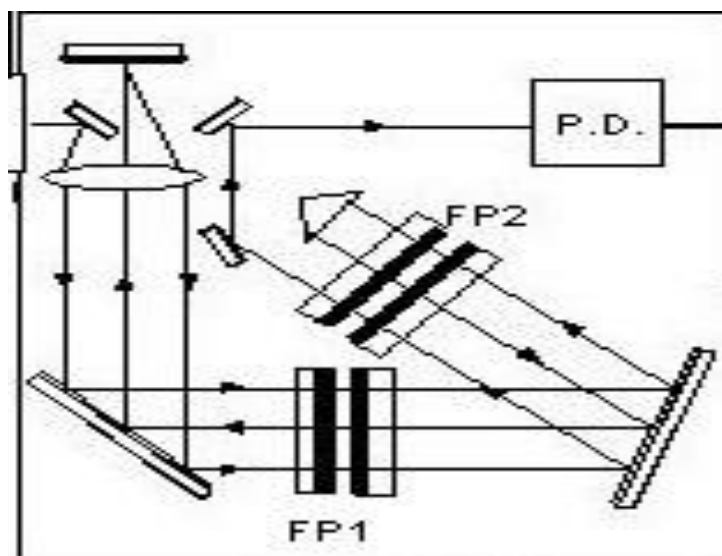


Fig. 3.4- Schematic view showing Fabry-Perot interferometers.

There are two different types of waves in which laser may interact with, either bulk acoustic waves (BAW) or surface acoustic waves (SAW). When bulk waves cannot be detected, such as in the case of opaque films, a suitable procedure for extracting information about the elastic properties of the coating from the observed SAWs is to be implemented. To this purpose, an optimized procedure has been developed in previous works. This procedure is based on a numerical computation, which, in turn, relies on statistical considerations.

For the sake of description, let us consider a typical Brillouin spectrum obtained for a metallic W coating on Si substrate, as the one shown in figure 3.5. The spectrum is plotted as a function of the measured acoustic waves velocity $v_m = \omega/k_{\parallel}$, where k_{\parallel} is the exchanged wavevector determined by the incidence angle of the laser onto the sample, ω is the angular frequency measured by the spectrometer.

Taking the shown spectrum as an example, several branches of the dispersion relation can be measured (i.e. the peaks present in the spectrum). Due to the opaque nature of the film, all the observed modes are surface acoustic waves. In particular, the lowest velocity branch is the Rayleigh wave (R), and the other branches are due to Sezawa waves (S).

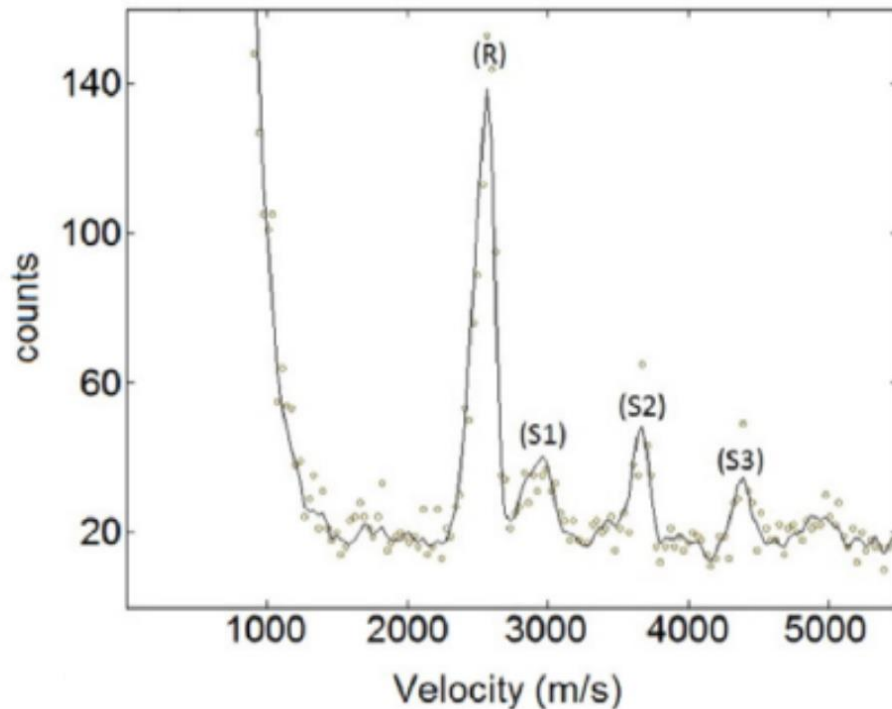


Fig. 3.5- Brillouin spectrum of metallic tungsten film.

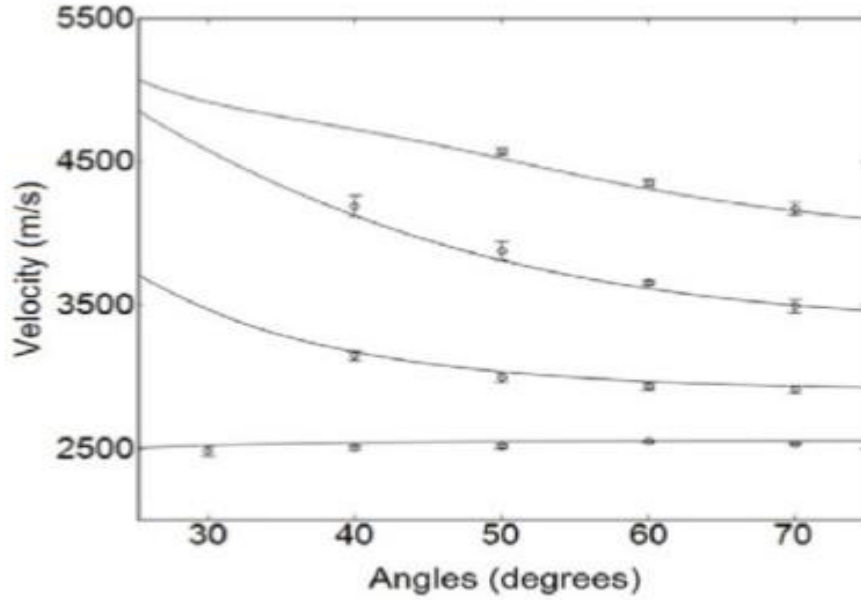


Fig. 3.6- Experimental and computed dispersion relation of a W film; curves are for the computed dispersion relations and dots are for the experimental velocities.

The analysis of the spectrum is done using a pre-written MATLAB code which is based on the minimization of least square estimator between the experimental and the computed numerical dispersion relation which are based on Christoffel's secular equations, which governs modes propagation as a function of different materials parameters, such as the mass densities of the film and the substrate ρ_f and ρ_s , the elastic constants of the film and the substrate (C_{ij}^f and C_{ij}^s), the film thickness t and the exchanged wavevector k_{\parallel} : $v_c = v_c(\rho_s, C_{ij}^s, \rho_f, C_{ij}^f, t|k_{\parallel}, j)$, see figure 3.6, reaching the elastic constants of the film with regions of different confidences, see figure 3.7.

$$LS(C_{ij}^f, \rho_f) = \sum_{j, k_{\parallel}} \frac{[v_c(C_{ij}^f, \rho_f | j, k_{\parallel}) - v_m(j, k_{\parallel})]^2}{\sigma^2(j, k_{\parallel})}$$

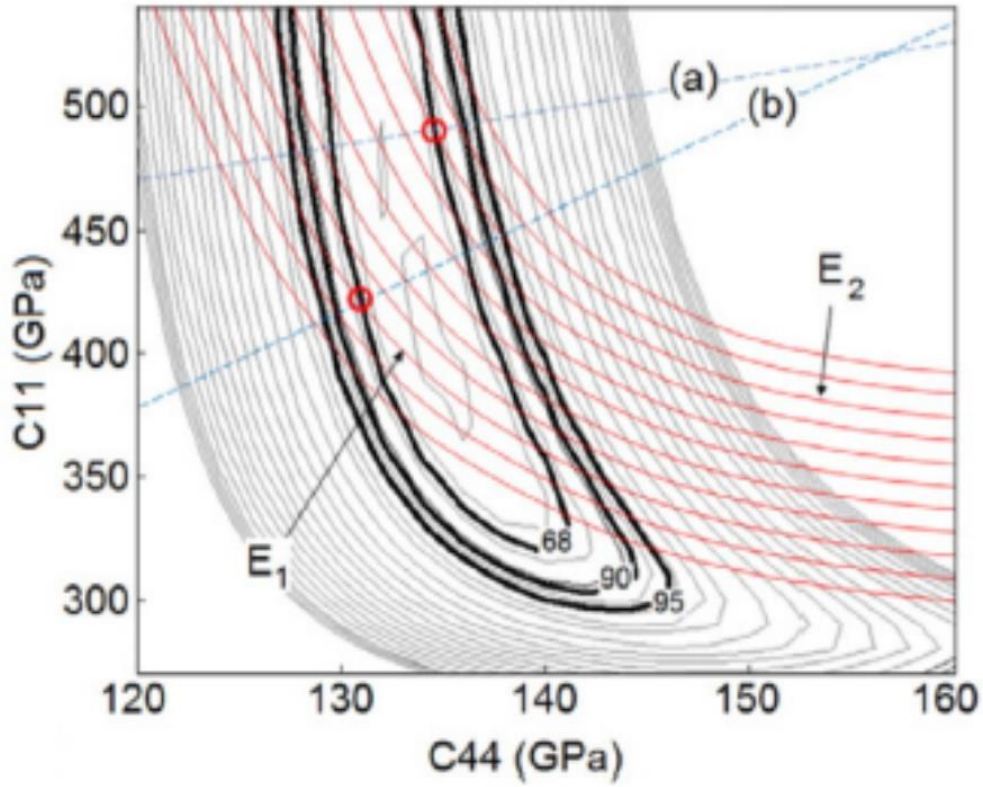


Fig. 3.7- Iso-level curves for the LS estimator; the bold black lines are curves corresponding to the 68%, 90% and 95% confidence regions. The lines (a) and (b) refer respectively to (K_{bulk}) and (G/K_{bulk}) . In red: iso-level curves for E . G and E are shear and Young's moduli respectively.

From the elastic constants the elastic moduli can be obtained as follows:

$$E = \frac{C_{44} \cdot (3C_{12} + 2C_{44})}{C_{12} + C_{44}}$$

$$\nu = \frac{C_{12}}{C_{12} + C_{11}}$$

$$B = \frac{C_{11} + 2C_{12}}{3}$$

$$G = C_{44}$$

3.3 Substrate Curvature Setup

In order to Investigate the thermal properties of coatings, namely coefficient of thermal expansion (CTE), an experimental setup, shown in figure 3.8, has been established to be coupled with Brillouin measurements.

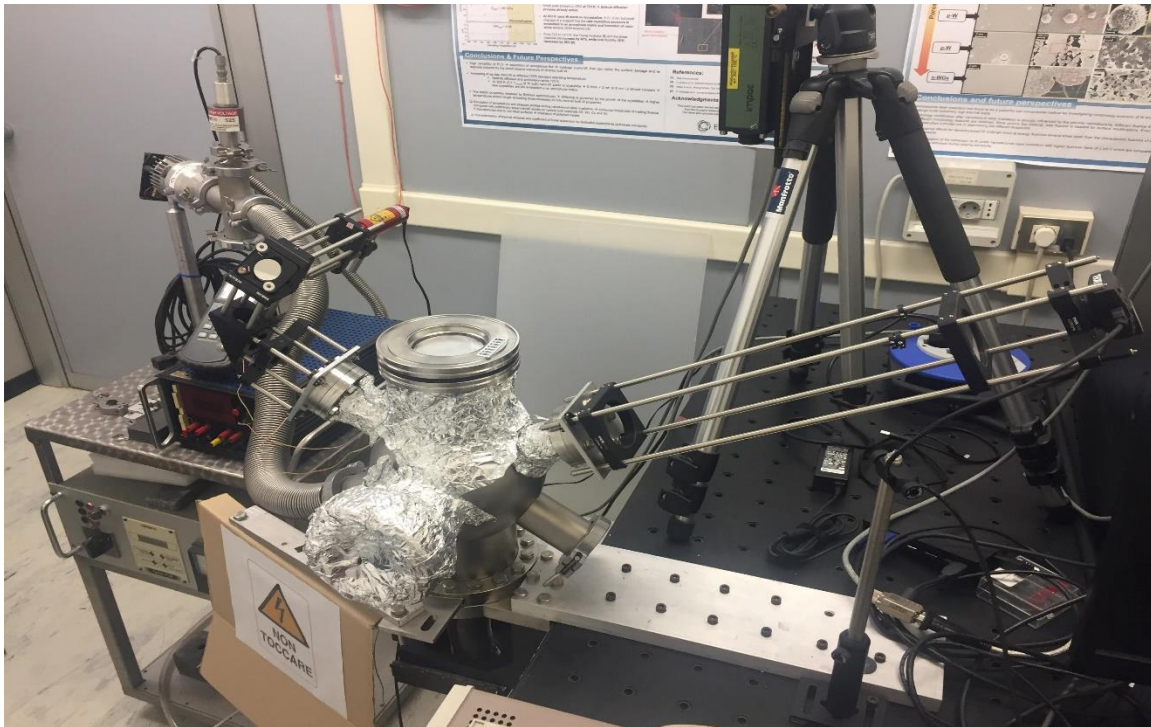


Fig. 3.8- Picture of curvature substrate experimental setup.

Coatings are subjected to residual stresses which arises mainly because of two reasons, one which is intrinsic due to the deposition process, where the ablated particles hit the substrate with certain kinetic energy, it may also be related to the mismatch between lattice parameters of both alumina and silicon substrate. The second reason, which is considered extrinsic, is related to the thermal expansion mismatch between the coating and the substrate rising when the sample is subjected to thermal cycle.

These stresses are intensified at the interface between coating and substrate which may lead to different failure scenarios of the samples such as cracking or delamination. Being able to detect and asses such stresses is extremely important to understand the limitations of our material and knowing the optimum conditions in which the failure of the coatings may not occur.

Coming to the technique itself, it has been developed recently at NanoLab of Politecnico di Milano to characterize CTE and to detect residual and thermal stresses using an optical source (laser) which is incident on the sample and then reflected to a camera sensor, see figure 3.9. The movement of the laser spots while heating the sample helps in exploring the curvature radius changes that happens due to different elastic and thermal properties of the coating and the substrate, see figures 3.10 a) and b).

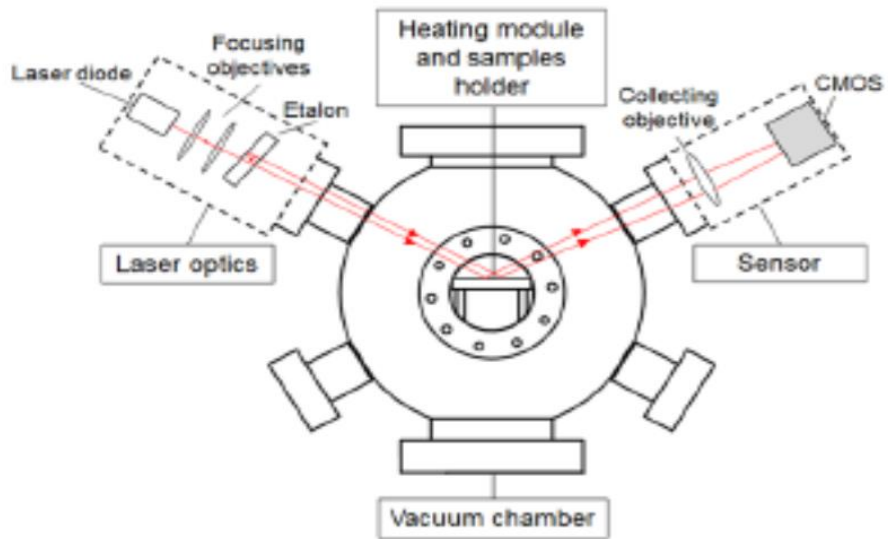


Fig. 3.9- Schematic view of the substrate curvature setup.

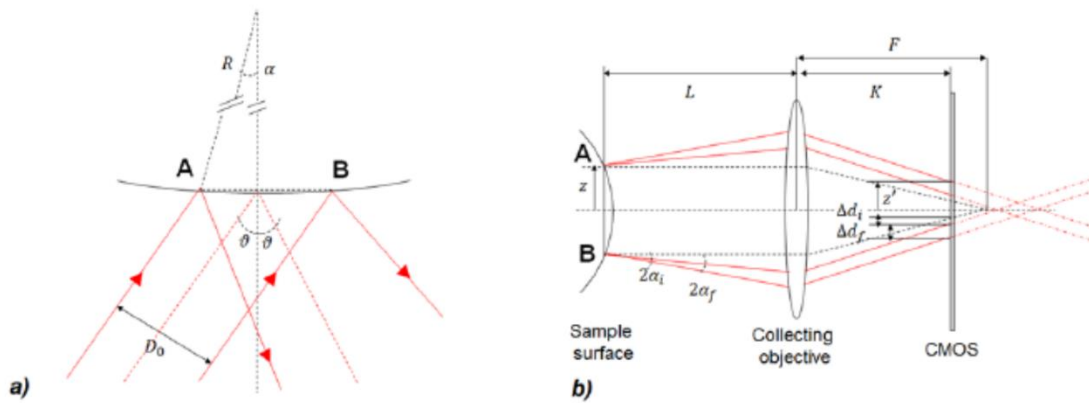


Fig. 3.10: a) Schematic representation of two initially parallel laser beams that are reflected by a curved surface. b) The reflected beams are collected by the collecting objective and recorded by the CMOS.

As can be noticed from the previous discussion, this setup is a non-destructive investigating technique, that makes it a powerful tool of investigation. It is also a versatile technique where both opaque and transparent coatings can be investigated.

If the samples are heated, the different thermal expansion behaviors between the coating and the substrate induce an additional bending to the system, that can be detected, as briefly discussed below, to obtain the CTE or to monitor the thermal stress evolution of the coating.

In the case of thin film deposited on a much thicker substrate, the stress within the film can be taken as approximately uniform, the stress within the coating can be expressed in terms of the bending curvature radius R by the well-known Stoney's equation [84,85]:

$$\sigma_f(T) = \frac{E_s}{1 - \nu_s} \frac{t_f}{t_s^2} \frac{1}{6} \left(\frac{1}{R(T)} - \frac{1}{R_o} \right)$$

Where the sub-indexes f and s stand for film and substrate respectively, $R(T)$ and R_o are the curvature radii at a certain temperature T and at a reference temperature T_o , while t is substrate or film thickness. The same equation may be used to measure residual stresses just by taking $R(T)$ and R_o as the curvature after and before deposition.

When thermal stresses arise upon heating or cooling due to a CTE mismatch between the coating and the substrate, the CTE of the coating can be deduced by the following equation:

$$CTE_f = CTE_s + \frac{d\sigma_f}{dT} \frac{1 - \nu_f}{E_f}$$

As can be seen from this equation, the elastic properties of the films must be known to obtain the CTEs. Here comes the coupling with Brillouin measurements, which consistently provides all the information about E_f and ν_f .

While writing the previous two equations, it was taken as an assumption that the elastic moduli are temperature independent, allowing to find a single value of CTE. Nevertheless, it is well known that the above properties show some temperature dependence. As a result, it would be better to take into consideration such temperature dependence of the elastic moduli of the substrate and the film and of CTE of substrate if a more detailed approach is to be conducted to find the temperature dependence of CTE of the film.

However, it is not an easy task to get the measurements of the temperature dependence of the elastic moduli of the coatings, unfortunately, it would be unavoidable to conduct such measurements if the explored temperature interval reaches either the melting temperature of the sample or any near to temperatures where phase transitions are to occur (recrystallization temperature).

It is worth mentioning that the measured CTE refers to the in-plane component of the linear thermal expansion coefficient. In anisotropic sample the in-plane component can significantly differ from the out of plane CTE, that must be determined by other techniques. The analysis of the acquired data is again done using a pre-written MATLAB code.

3.4 Preparation of Al₂O₃ & Y₂O₃ Samples

As mentioned previously, PLD has been used as the deposition technique for both Al₂O₃ and Y₂O₃ coatings on silicon substrates. Eight different alumina samples have been produced, alongside, several other yttria samples at Istituto Italiano di Tecnologia (IIT) in Milan.

The deposition of the coatings was done in a stainless-steel vacuum chamber at low oxygen pressure of around 0.15 Pa on one face of the silicon substrates, at room temperature. The energy of the laser pulse was at 250 mJ, whereas the focus was adjusted to a fluence of 2.38 J/cm², with a repetition rate of 20 Hz.

For alumina, each two samples have been deposited with different thickness as follows, 2 μm , 1 μm , 500 nm and 250 nm, depending on the number of laser pulses, the rate of deposition was roughly 1 nm/s. In addition, silicon substrates having a thickness of 500 μm to ensure the maximum sensitivity during the curvature measurements.

Now that the samples are ready, the steps taken to study them are as follows, first, residual stresses, which arise intrinsically because of the deposition process itself, are to be measured via the substrate curvature setup.

As a second step, each two samples of the same material with a similar thickness are to be used in a different experiment, e.g. one in Brillouin spectroscopy and the other in the substrate curvature setup, for the sake of saving time. That will allow us to get information about elastic constants alongside CTE.

Two of alumina samples, 2 μm and 1 μm , will get annealed at a temperature of 750 °C for 20 minutes. γ -alumina phase, for PLD-grown samples, starts forming around that temperature.

Elastic moduli of the two annealed samples are to be measured to compare them with the ones of as-deposit alumina.

For yttria, several samples have been provided having various thicknesses as follows, 2 μm , 1 μm and 500 nm, they were deposited on 500 μm silicon substrates. Yttria samples have been limitedly investigated, getting only several frequency spectra, alongside residual stresses within the coatings.

We expect at the end to have information on the residual stresses, elastic moduli and CTEs of as-deposit samples after going through the previously mentioned steps. Furthermore, information about elastic moduli of annealed Al₂O₃, γ -alumina phase, will be acquired.

4. Thermo-Mechanical Assessment of Al₂O₃ Coatings

Throughout this chapter, the results of the different measurements and thermo-mechanical behavior of the different coatings are to be shown.

4.1 Residual Stresses

There are mainly two reasons of the presence of residual stresses within the samples, one is intrinsic related to the deposition process itself, represented by the bombardment of high energetic particles onto the substrate, and the lattice parameter mismatch between the film and the substrate. The second reason is an extrinsic one which is related to the different CTEs of the film and substrate under thermal loads.

After preparing all the samples, we start by measuring the curvature of the bare substrate several times for each to minimize any statistical uncertainty, and then taking the same measurements for the samples after deposition and use the previously mentioned Stoney's equation to get the residual stresses.

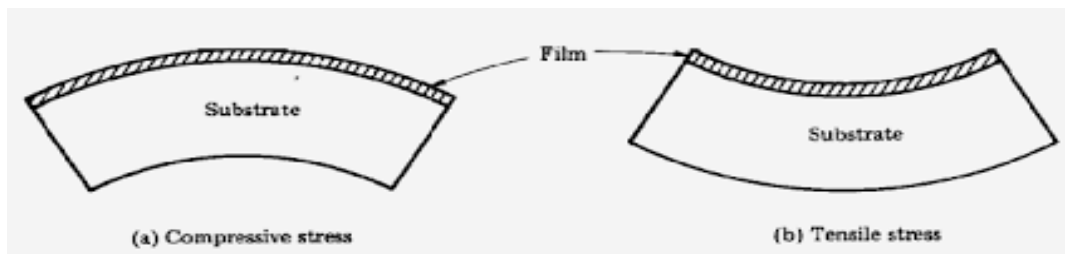


Fig. 4.1: a) Compressive stress within the film. b) Tensile stress within the film.

During deposition of the film, compressive stress starts rising within the film as a result of the expansion process of the film itself which is resisted by the substrate, the sample starts taking a convex shape [99], see figures 4.1a) and 4.2 which views it in a detailed manner.

The other way around is that tensile residual stress arises within the film as a result of the CTE mismatch of the film and the substrate under thermal loads, the film having the lower CTE, the sample starts taking a concave shape caused by the force introduced by the physical boundaries of the substrate itself, considering, see figure 4.1b).

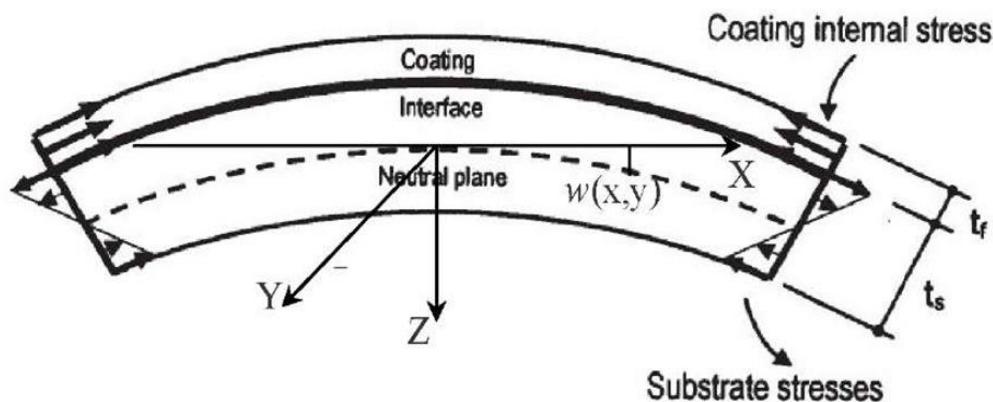


Fig. 4.2- Compressive stress arises within the coating as a result of the substrate bending.

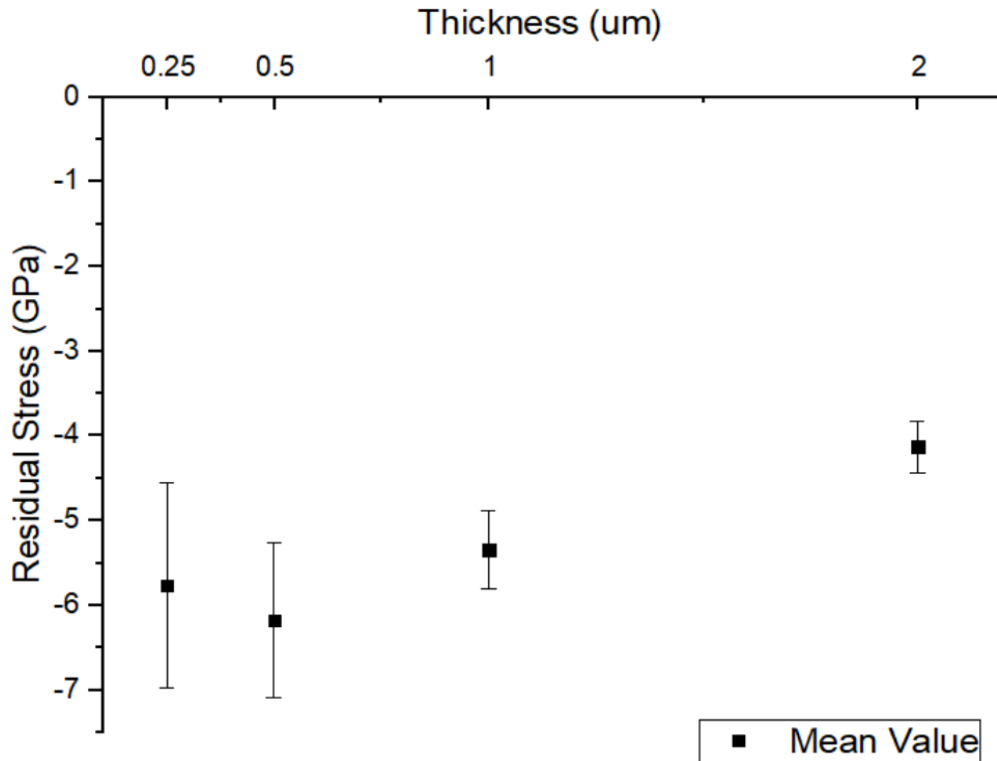


Fig. 4.3- Plot of residual stress with film thickness.

Figure 4.3 shows the results acquired from the substrate curvature setup measuring the residual stresses of the samples. A trend of high compressive residual stress is shown for all the films with lower thicknesses which then reduces with increasing the thickness, except for the 250 nm sample which is believed to be related to the high error bars of the thinner films.

This result matches the theory that compressive stress, which arises because of film expansion, is highest for low thicknesses and then relaxes by the presence of defects which are increased in the number with increased thicknesses, till a point where it may convert from compressive residual stress to a tensile one passing through zero residual stress point [99].

Furthermore, the magnitudes of the residual stresses, shown in figure 4.3, are so high as can also be seen from the plot, the reason behind that may be related to the way substrates were fixed to the holder while depositing the samples, as they were fixed using a cartoon tape going all around the frame of each of them, introducing an extra force, which increases the stress within the film.

Shown in figure 4.4, data acquired by both Edoardo Besozzi (department of Energy, Politecnico di Milano), which shows the thickness at which the conversion, from compressive stress to tensile stress, happens.

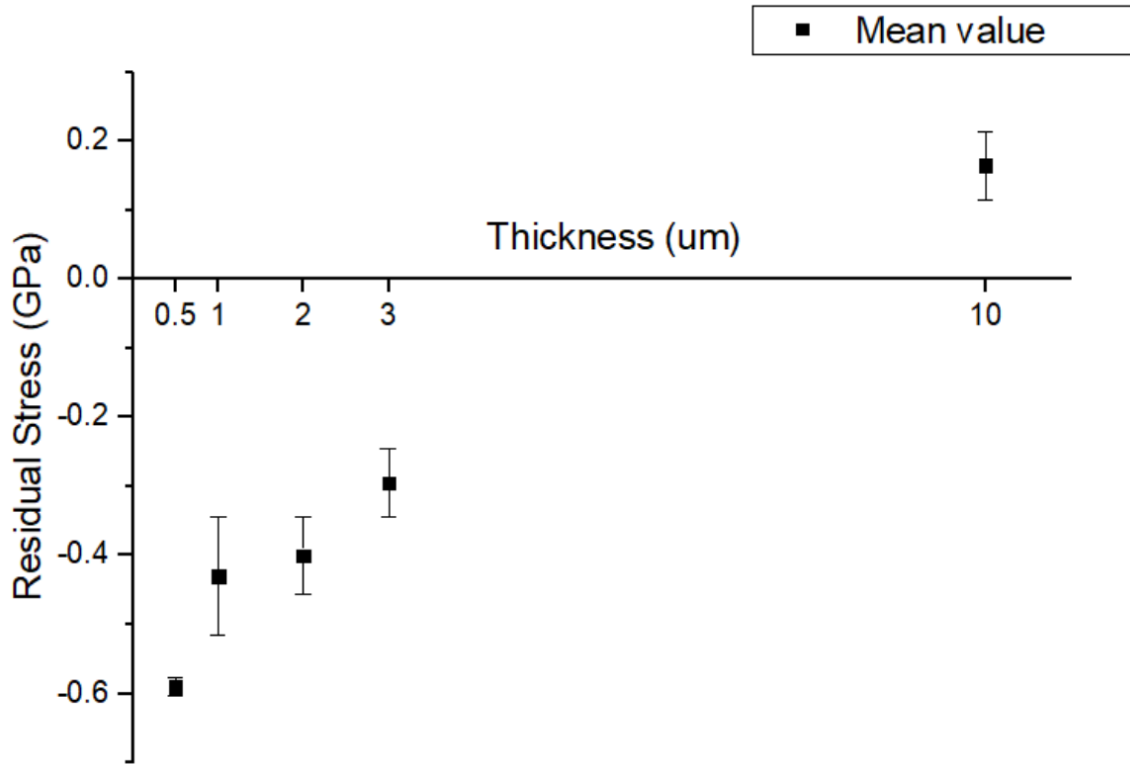


Fig. 4.4– Plot showing the change from compressive to tensile residual stress with respect to film thickness.

4.2 Elastic Moduli

As mentioned in the previous chapter while discussing the concept of Brillouin spectroscopy, elastic moduli of the different samples can be acquired. Elastic moduli depend mainly on the microstructure, morphology, atomic density and strength of the atomic bonds, as a matter of fact, higher elastic moduli would be expected with higher atomic densities and certainly with stronger atomic bonds. It is not obvious if thickness of the films would have a direct effect on the elastic moduli or whether it affects them in an indirect way.

Considering different scenarios while depositing the films may clarify this point, taking as an example a thin alumina film, which grows on silicon substrate. At some thickness point, the morphology of the film will start changing from compact amorphous to some sort of columnar microstructures, with higher atomic density in the vertical direction and a lower one in the lateral direction, an anisotropic material with different elastic moduli with different directions.

It may also happen during the film growth that the particles ablated from the target material start forming agglomerating before reaching the substrate forming nano-crystalline grains with a better atomic packing factor, and as a result, higher elastic moduli.

It turned out that it is not possible to predict what would happen with higher thicknesses, considering that elastic moduli depend highly on the conditions of deposition and on the deposition technique itself.

Not only they depend on the technique, but it is also expected to find different elastic moduli depending on whether the sample is as-deposited or whether it went through thermal cycles (annealed). In this case, it can be expected what kind of results we may get, since it is well known that samples going through thermal loads start to crystallize at different temperatures depending on the type of the material, crystallized materials have atoms which are well packed together, that increases the atomic density and as a consequence increasing elastic moduli.

In other words, one would expect samples with higher mass densities to have higher elastic moduli and better features to withstand the tough environment inside the reactor core, while elastic moduli of samples with different thicknesses cannot be predicted and measurements are needed to be conducted to assess them.

Figures (4.5-4.8) show the different maps of the elastic constants (C_{11}, C_{44}) acquired by the least square method using MATLAB code, where the abscissa is C_{44} and the ordinate is C_{11} , while the red curves are iso-levels of Poisson's ratio, where the thicker curve is the one corresponding to Poisson ratio equal to zero.

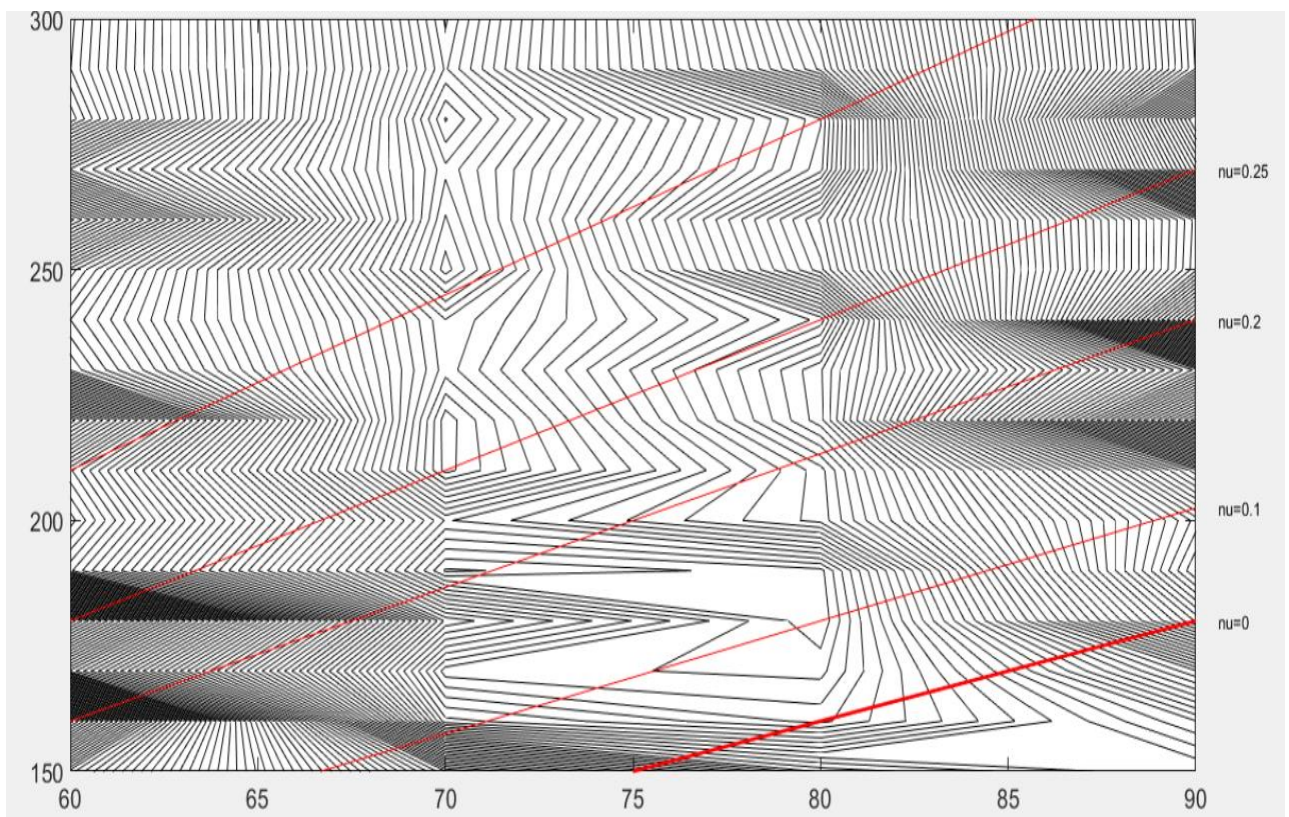


Fig. 4.5- The least square map for the 250 nm sample.

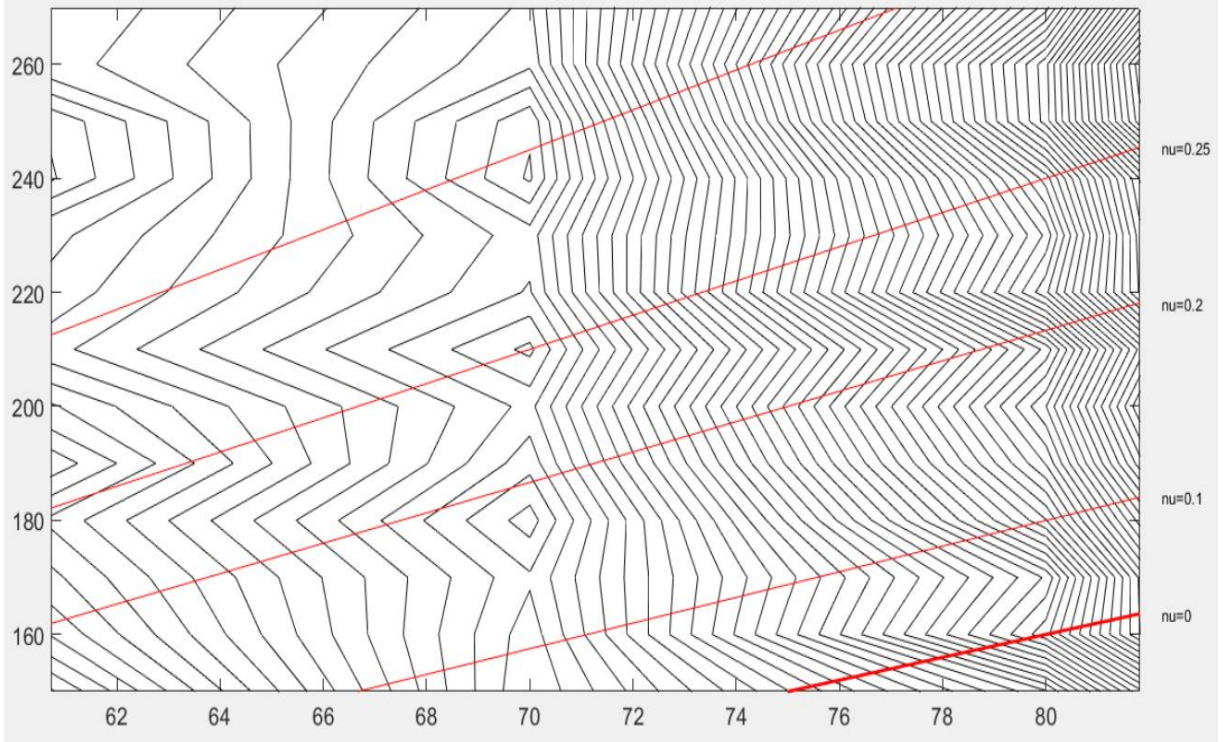


Fig. 4.6- The least square map for the 500 nm sample.

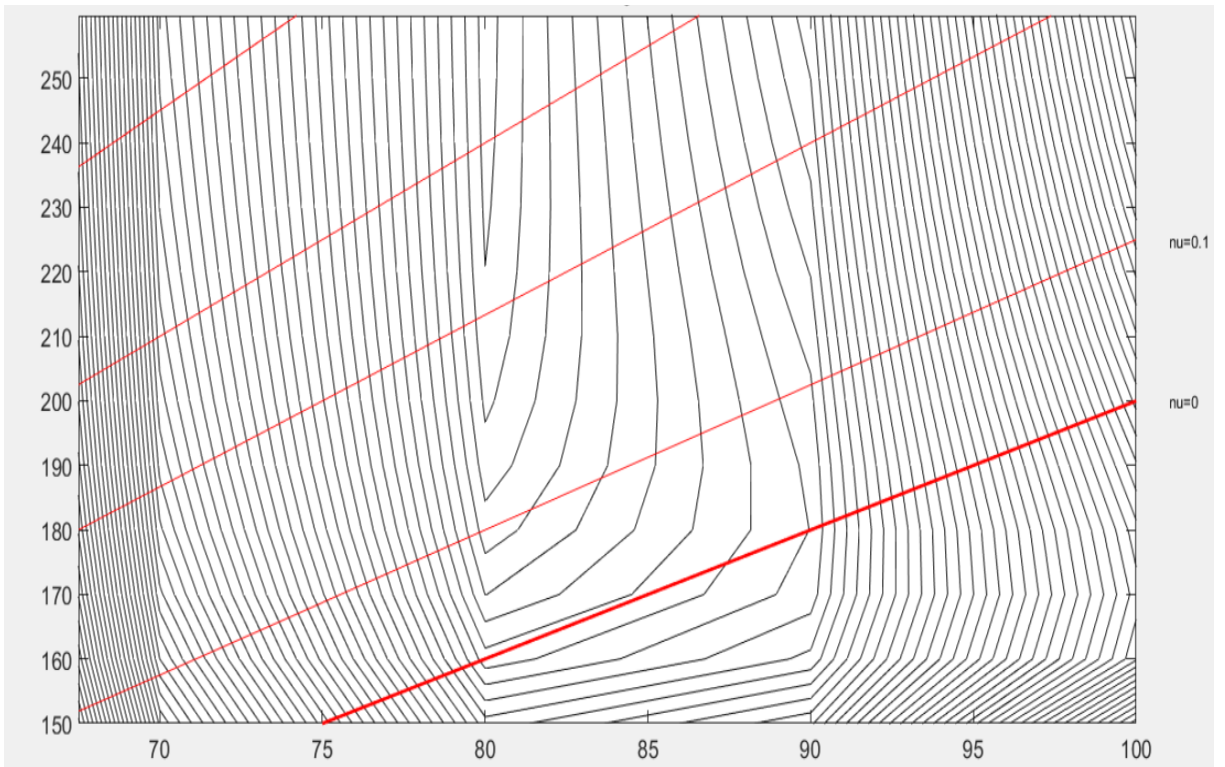


Fig. 4.7- The least square map for the 1 μm sample.

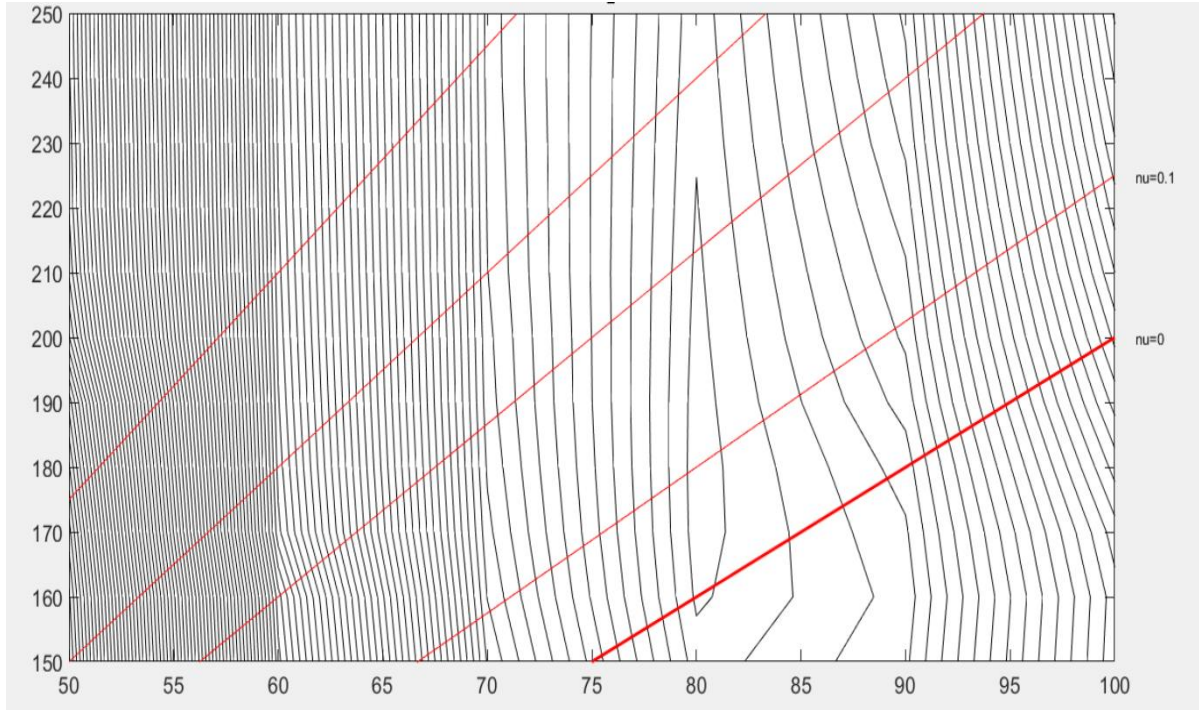


Fig. 4.8- The least square map for the 2 μm sample.

As can be seen from the maps, the minimum of C_{44} is in a good shape since it is quite definite for the four samples, it is around 70 GPa for the 250 nm and the 500 nm samples and around 80 GPa for the 1 μm and 2 μm samples. While the minimum for C_{11} is in a bad shape, since either multiple minimums or minimum with very high uncertainties.

That is not surprising, since the surface elastic waves we detect have a velocity which is so close to the velocity of the bulk shear waves, C_{44} which is equal to the shear modulus (G), may be calculated knowing the velocity of the shear wave and the mass density. While C_{11} is related to the velocity of the bulk longitudinal waves and can be calculated using it and the mass density.

$$v_l = \sqrt{\frac{C_{11}}{\rho}} \qquad v_s = \sqrt{\frac{C_{44}}{\rho}}$$

For the two thicker samples it was possible to detect the bulk longitudinal waves and to indicate its velocity. Considering the velocity of the shear waves, it can be taken to be approximately equal to the velocity of the Rayleigh wave.

The two elastic constants can now be calculated knowing the mass density of the samples, which is calculated using Lorentz-Lorenz equation [69]. These data were presented in a scientific paper, where alumina films were deposited in the same conditions as the ones considered here.

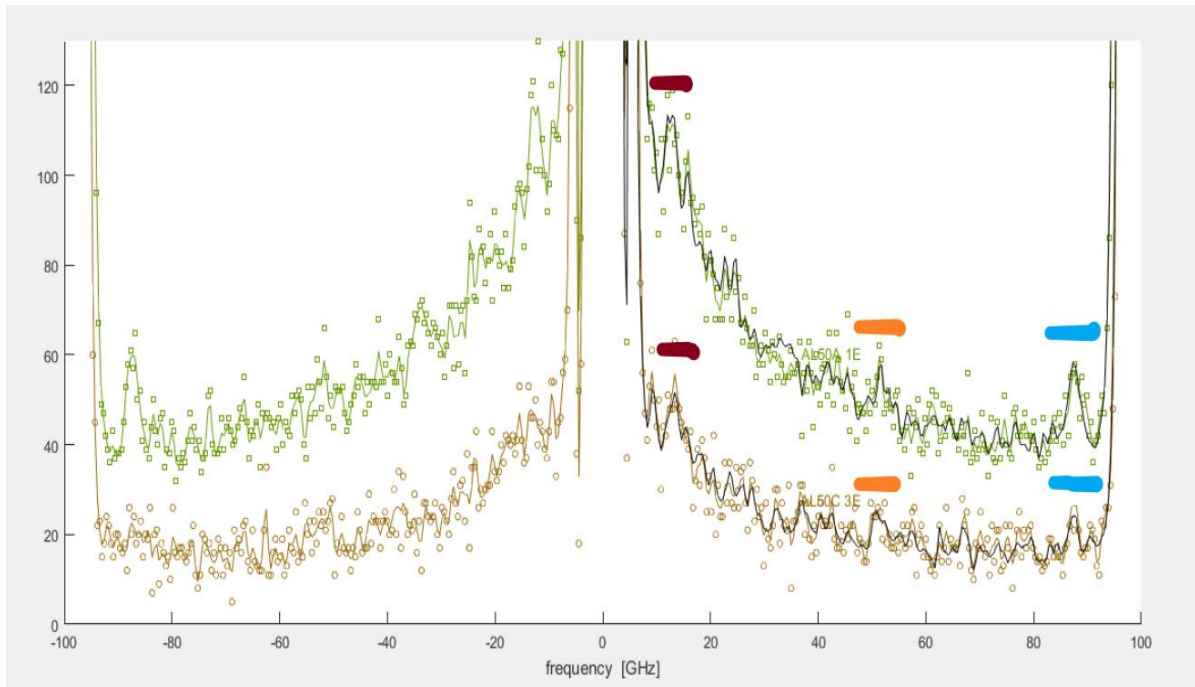


Fig. 4.9- Frequency spectra for the $1 \mu\text{m}$ and $2 \mu\text{m}$ samples, below and above respectively, with laser incident angle of 50° . Shown under the colored lines, Rayleigh wave, bulk longitudinal wave of the film and bulk transverse wave of the substrate, respectively from left to right.

Figure 4.9 shows two frequency spectra of the two thicker samples, the upper one corresponding to the $2 \mu\text{m}$ sample and the lower one to the $1 \mu\text{m}$ sample. The peaks colored with brown, orange and blue lines above each of them are Rayleigh wave of the film, bulk longitudinal wave of the film and bulk transverse wave of silicon substrate, respectively. Being able to detect bulk transverse for the lower silicon layer tells us that our samples are transparent to the incident laser beam.

The situation is not that easy with the thinner samples since it is not possible to detect any bulk waves and as a result, a different approach should be considered. Knowing that it is impossible to find alumina with higher bulk's modulus (B) than sapphire, which is a single crystal alumina, while at the same time it is not possible to find Poisson's ratio (ν) which is lower than that of sapphire, table 4.1 shows the mechanical properties of sapphire.

Those two facts put a higher and lower limit for C_{11} of the two thinner films, which allows us to get the elastic moduli with the previously known C_{44} from the maps, but nevertheless, those higher and lower limits are quite separate and thus will give us a huge uncertainty for the values of E .

Here comes one more step to enhance the results even further, expecting that the four different samples to have, more or less, the same mechanical properties since they were deposited in exactly the same conditions, that gives us an opportunity to just investigate the values of C_{11} of which are in the vicinity of the computed values of the thicker samples.

By doing so, that gave us a reasonable result of the dispersion relations of the two thinner samples, see figures 4.10 and 4.11 for better illustration.

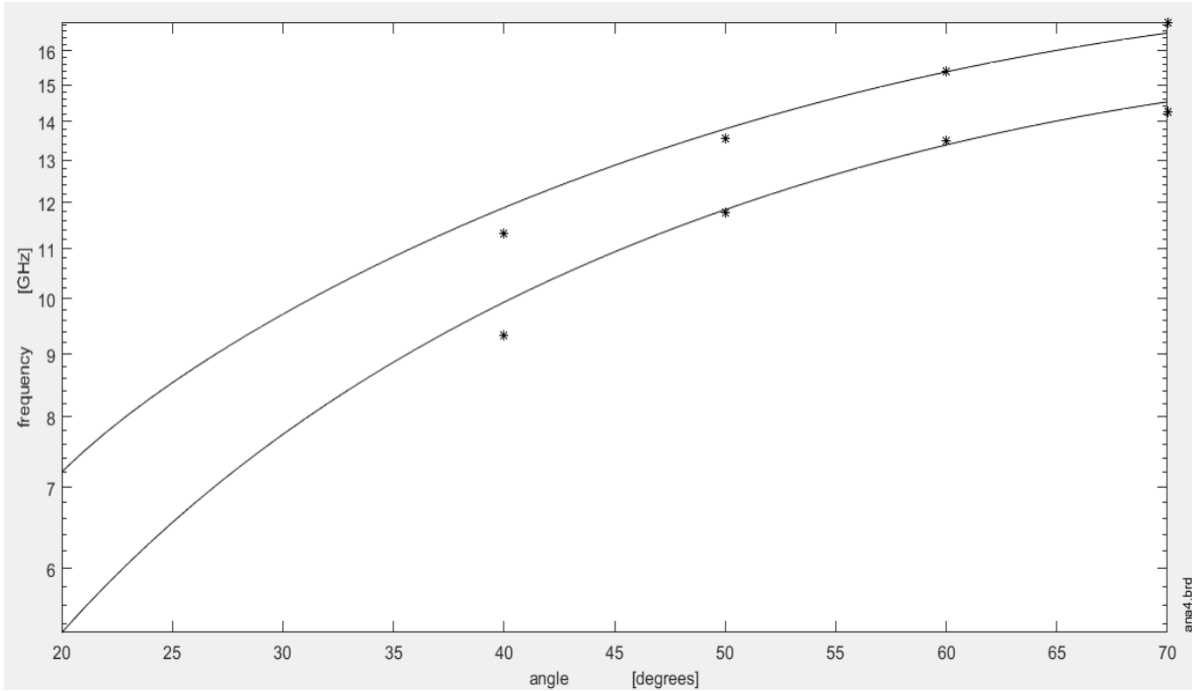


Fig. 4.10- Computed dispersion curves for the 500 nm sample, using C11 values close to the ones of the thicker samples, and the points are the experimental frequencies at different incident angles.

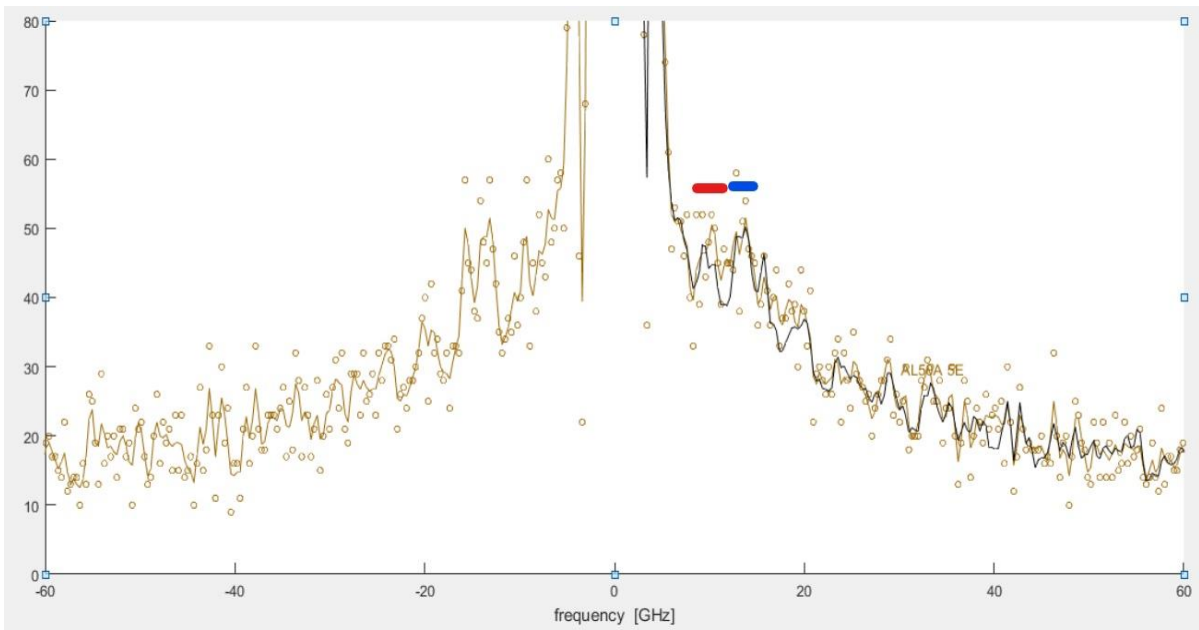


Fig. 4.11- The two experimental points for the 500 nm sample at 50° incident angle, taken in the previous figure, under red and blue lines, corresponding to Rayleigh and Sezawa waves, respectively.

Tables (4.2-4.5) summarize the results acquired for the four different thicknesses. Figure 4.12 shows a plot of Young's moduli with the different thicknesses. As can be noticed from the plot, Young's moduli of the different samples are in the same vicinity as expected and are also compatible with previous results acquired for alumina samples deposited under the same conditions, the study was done by Francisco Garcí'a Ferre et al [69]. Considering that the samples were deposited under the same conditions, those results are not at all surprising. Figure 435 shows the plot of the different thicknesses with Poisson's ratios, they are varying slightly with thickness and are almost fine with the results of Ferre.

Table 4.1

Mass density ρ , Young's modulus E , Poisson ratio ν , bulk modulus B and shear modulus G of sapphire [97].

ρ ($g * cm^{-3}$)	3.98
E (GPa)	345
ν	0.25 - 0.3
B (GPa)	250
G (GPa)	145

Table 4.2

Young's modulus E , Poisson ratio ν , bulk modulus B , shear modulus G and elastic constants (C_{11} , C_{44}) values of the 250 nm sample, the column on the right corresponds to the standard deviation from the mean value.

E (GPa)	181	± 4
ν	0.26	± 0.1
B (GPa)	124	± 9
G (GPa) = C_{44}	72	± 1
C_{11}	220	± 10

Table 4.3

Young's modulus E , Poisson ratio ν , bulk modulus B , shear modulus G and elastic constants (C_{11} , C_{44}) values of the 500 nm sample, the column on the right corresponds to the standard deviation from the mean value.

E (GPa)	181	± 6
ν	0.27	± 0.1
B (GPa)	135	± 19
G (GPa) = C_{44}	71	± 1
C_{11}	230	± 20

Table 4.4

Young's modulus E , Poisson ratio ν , bulk modulus B , shear modulus G and elastic constants (C_{11} , C_{44}) values of the 1 μm sample, the column on the right corresponds to the standard deviation from the mean value.

E (GPa)	195	± 4
ν	0.26	± 0.01
B (GPa)	136	± 7
G (GPa) = C_{44}	77	± 1
C_{11}	239	± 5

Table 4.5

Young's modulus E , Poisson ratio ν , bulk modulus B , shear modulus G and elastic constants (C_{11} , C_{44}) values of the 2 μm sample, the column on the right corresponds to the standard deviation from the mean value.

E (GPa)	187	± 4
ν	0.28	± 0.01
B (GPa)	143	± 8
G (GPa) = C_{44}	73	± 2
C_{11}	240	± 6

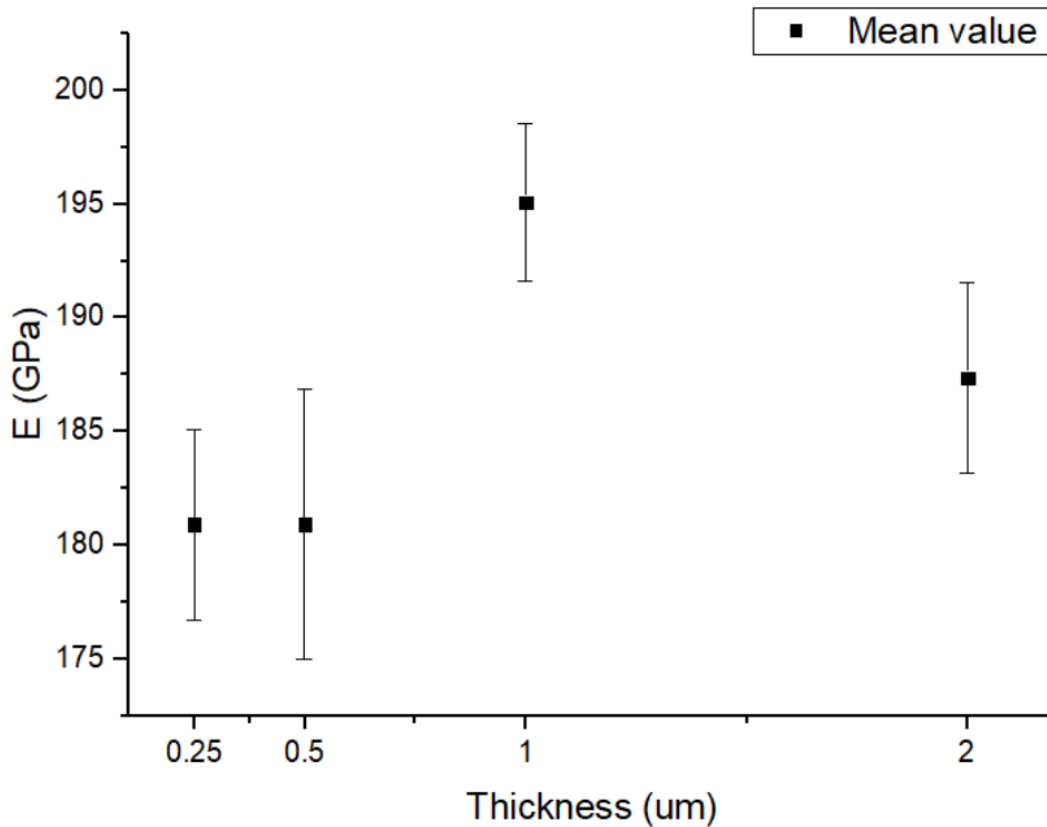


Fig. 4.12- Plot of Young's modulus of as-deposit samples with thickness.

4.3 Coefficient of Thermal Expansion (CTE)

Now that the different elastic moduli of the samples are known, it is quite possible, as mentioned before, to couple the setup of substrate curvature with Brillouin spectroscopy and get information about CTEs of the different samples.

The approach to do so is to get the sample into the furnace chamber of the setup, and then increasing the temperature till ~ 600 °C and then cooling it down till relatively low temperature and going back again to 600 °C and finally cooling it down to a low temperature. The reason of doing such thermal cycle is to make sure if any kind of microstructural change has occurred, and whether this change is repeatable or not.

It is well known that in general, the CTE of alumina is higher than that of silicon ($\sim 3.3 \times 10^{-6} \text{C}^{-1}$ around the temperature of 300 °C), which means that under thermal loads we expect a higher rate of expansion for alumina than silicon and the sample will start taking a convex shape, or if it is already in a concave shape it will start straightening. This also means that some compressive stresses will arise because of the physical boundary represented by the silicon substrate itself, providing a force which counters the expansion of the film.

From the equation linking E with CTE mentioned in the previous chapter, we expect that the results of the CTEs will go in an opposite manner with those of E , since, as previously mentioned, higher young's modulus means stronger atomic bonds and higher atomic density, as a result, that leads to lower CTE.

Shown in figures (4.13-4.16) the thermal cycles for the different samples, where the abscissa is the temperature of the sample and the ordinate is the residual stress evolution during the thermal cycles, the red line are linear fits to get the slope of the initial part of the curve.

As can be seen from the figures, compressive stress arises at the beginning which is compatible with what we predicted knowing that CTE of the alumina film is higher than the CTE of the silicon substrate.

Furthermore, there are temperature points in the different curves where some sort of a transition happens, these transitions work in reducing the compressive stress within the film and moving towards altering it into tensile one.

The hypothesis reached to justify this behavior is that the samples start to relax at some temperature and the atoms forming the thin films start moving and relocating their positions into new ones until an equilibrium is reached. The transition temperature is slightly different from one sample to another and that may be related to the magnitude of the residual stresses held within the sample itself.

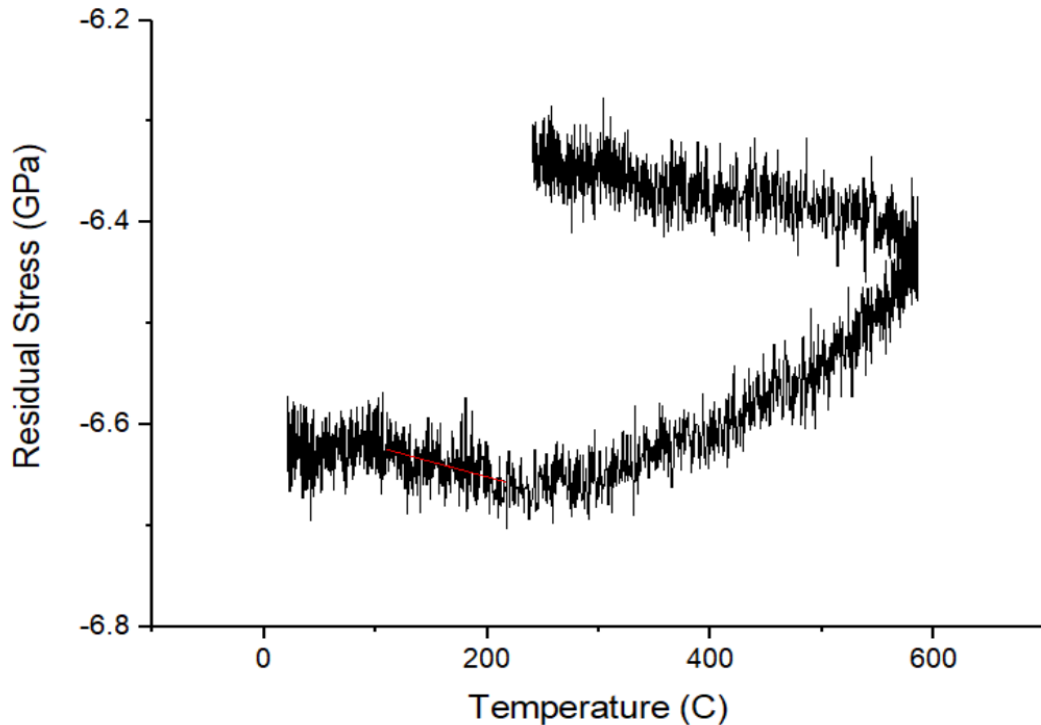


Fig. 4.13- The change of residual stress of the 250 nm sample with temperature.

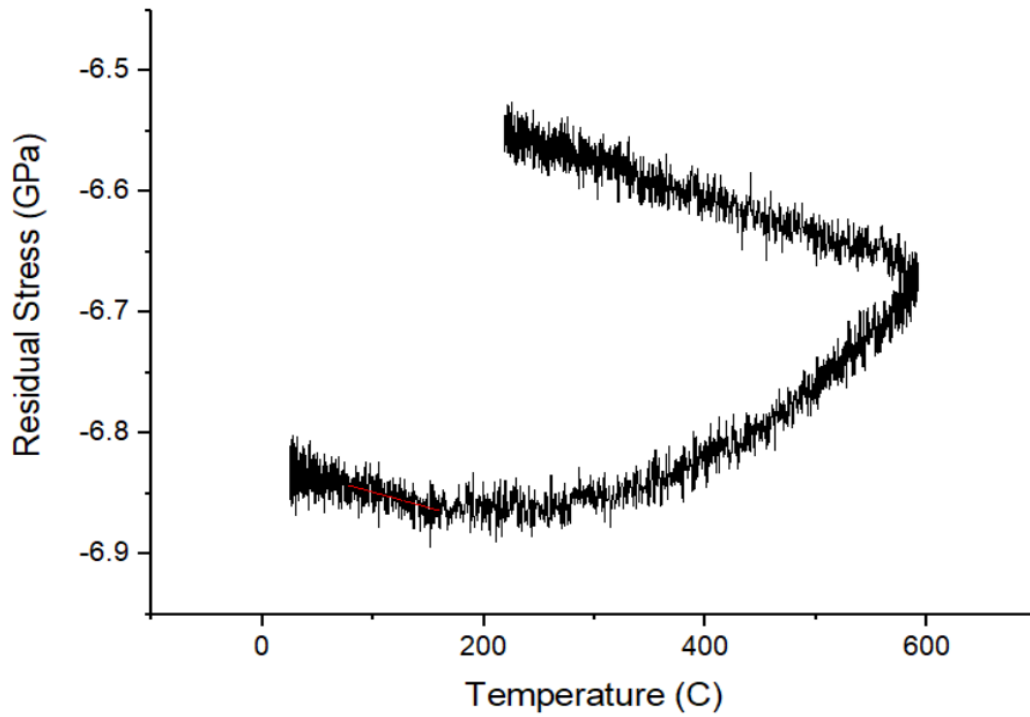


Fig. 4.14- The change of residual stress of the 500 *nm* sample with temperature.

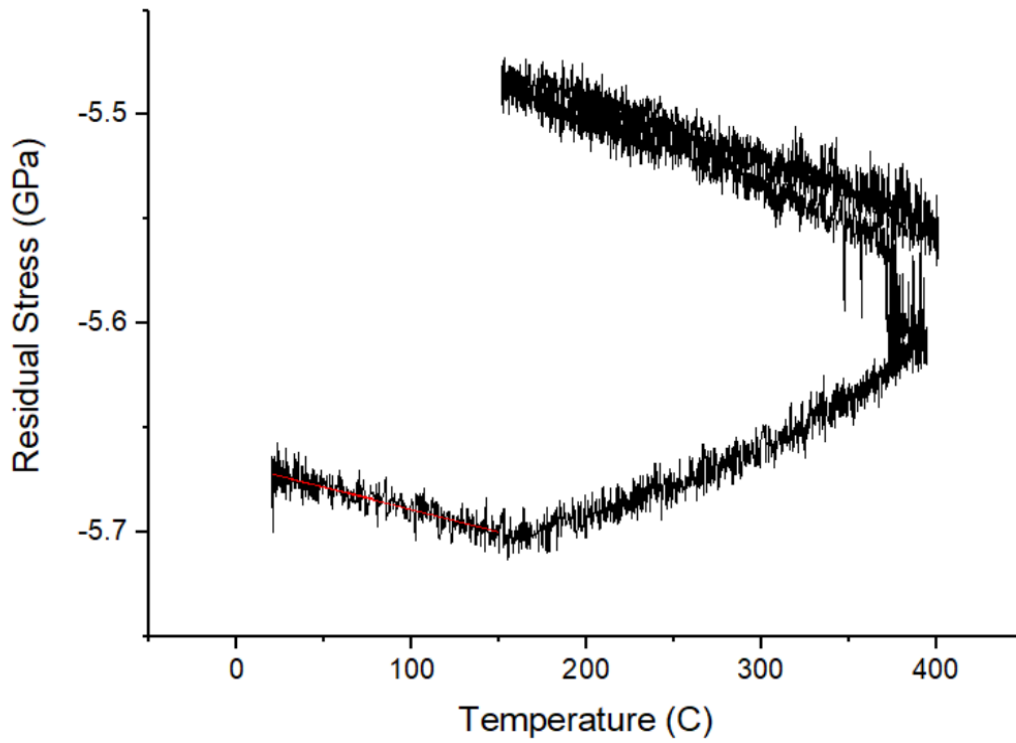


Fig. 4.15- The change of residual stress of the 1 μm sample with temperature.

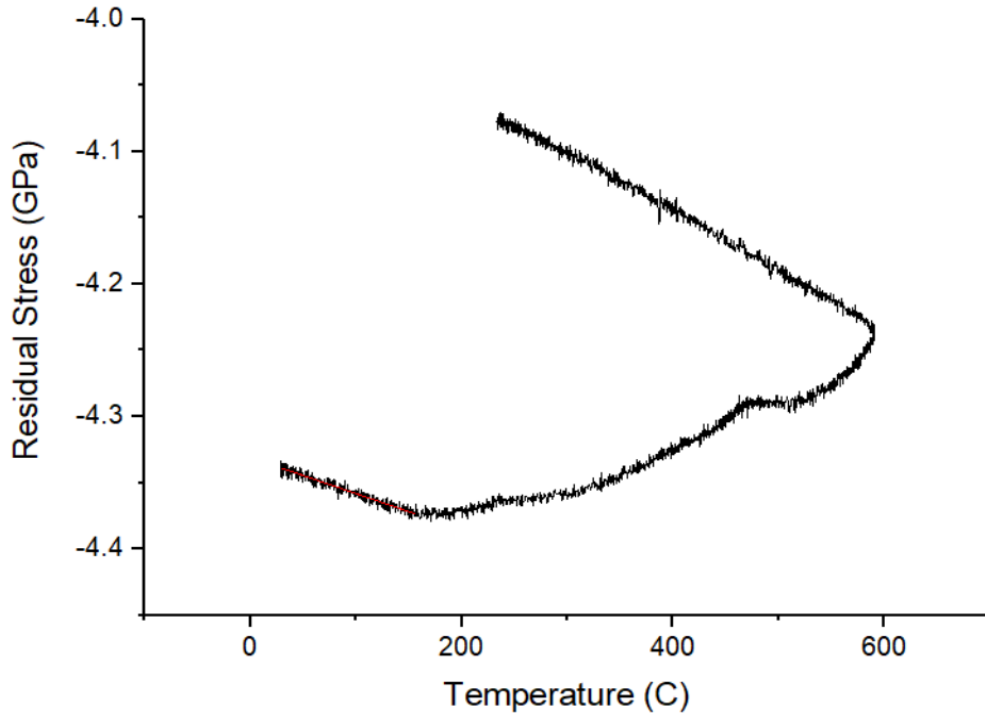


Fig. 4.16- The change of residual stress of the 2 μm sample with temperature.

Being able to get the slope of each curve and having E for different films, it is possible to get CTEs of the films. Figure 4.17 shows a plot between the measured CTEs of the different samples with thickness, and as expected, the trend went with an opposite manner of that of E . Depending on whether the film is as-deposit or annealed, one would expect some changes in the CTE of the film as well. But unfortunately, we had no chance to do such study in this thesis work.

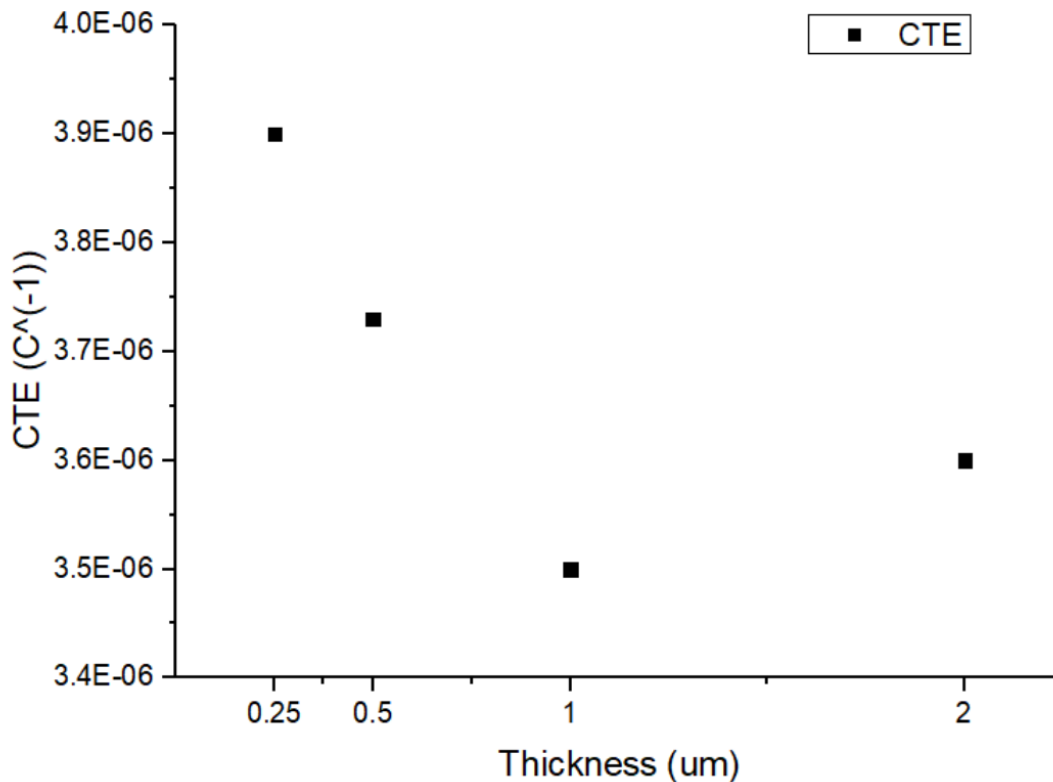


Fig. 4.17- Plot of coefficient of thermal expansion with thickness.

4.4 Elastic Moduli for Annealed Al₂O₃

As previously mentioned, the 2 μm and 1 μm samples have gone through an annealing process at around 750 °C for 45 minutes for the 1 μm sample and 30 minutes for the 2 μm samples. Figures (4.18-4.20) show an XRD patterns, acquired at (IIT, Milan), for 500 nm, 1 μm and 2 μm samples, respectively, annealed at different temperatures for 12 hours in each case, where the different samples start to crystallize at different temperatures.

For the 500 nm sample, the crystallization starts somewhere between 700 °C and 750 °C, which is already higher than the other two cases where it starts around 680 °C for 1 μm sample and at even lower temperature for 2 μm one. The hypothesis introduced for this discrepancy is that with higher thicknesses there is bigger volume that the atoms of the film can relocate and reorient themselves into new equilibrium positions with a lower thermal energy, while for the thin sample, its bulk volume is quite small that to introduce any kind of change in the microstructure or morphology of the film, it will require a slightly higher thermal energy than in the case of thicker films.

The region surrounded by the yellow circle in the XRD of 1 μm sample is showing a behavior which is thought to be a metastable alumina phase, considering the changes which happen in the XRD at that region. For the 1 μm and 2 μm samples, the peaks get more intense and the contrast gets better with increasing the annealing temperature, as of course expected.

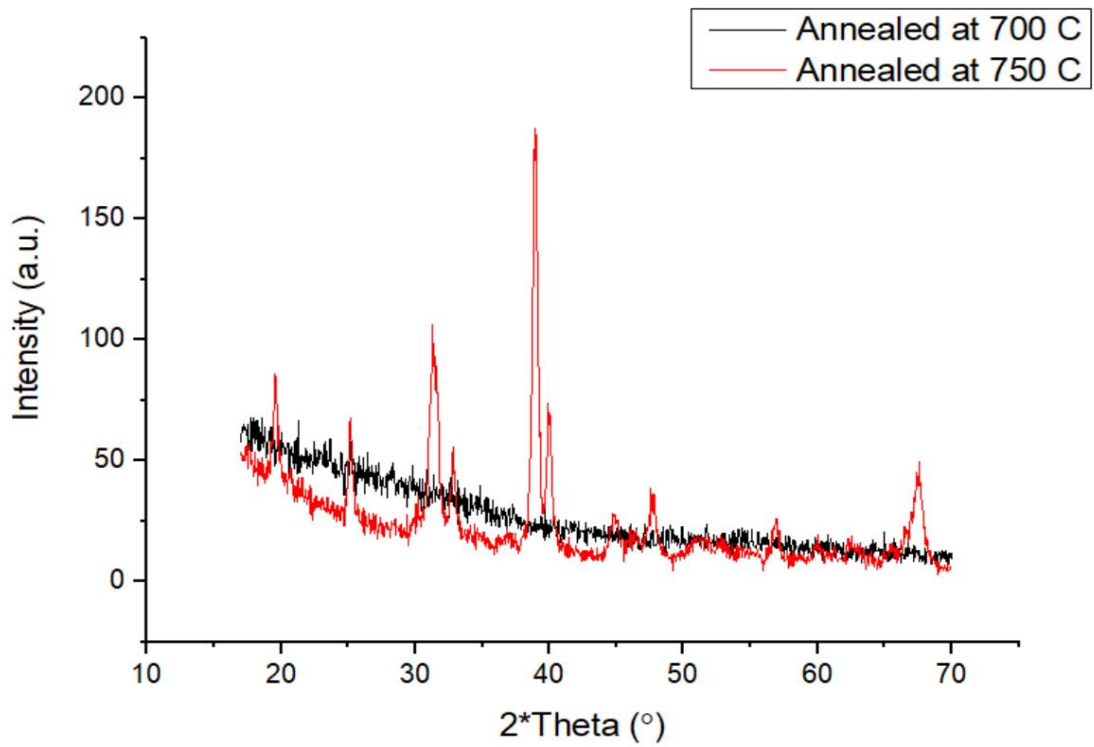


Fig. 4.18- XRD for 500 nm sample annealed at different temperatures for 12 h.

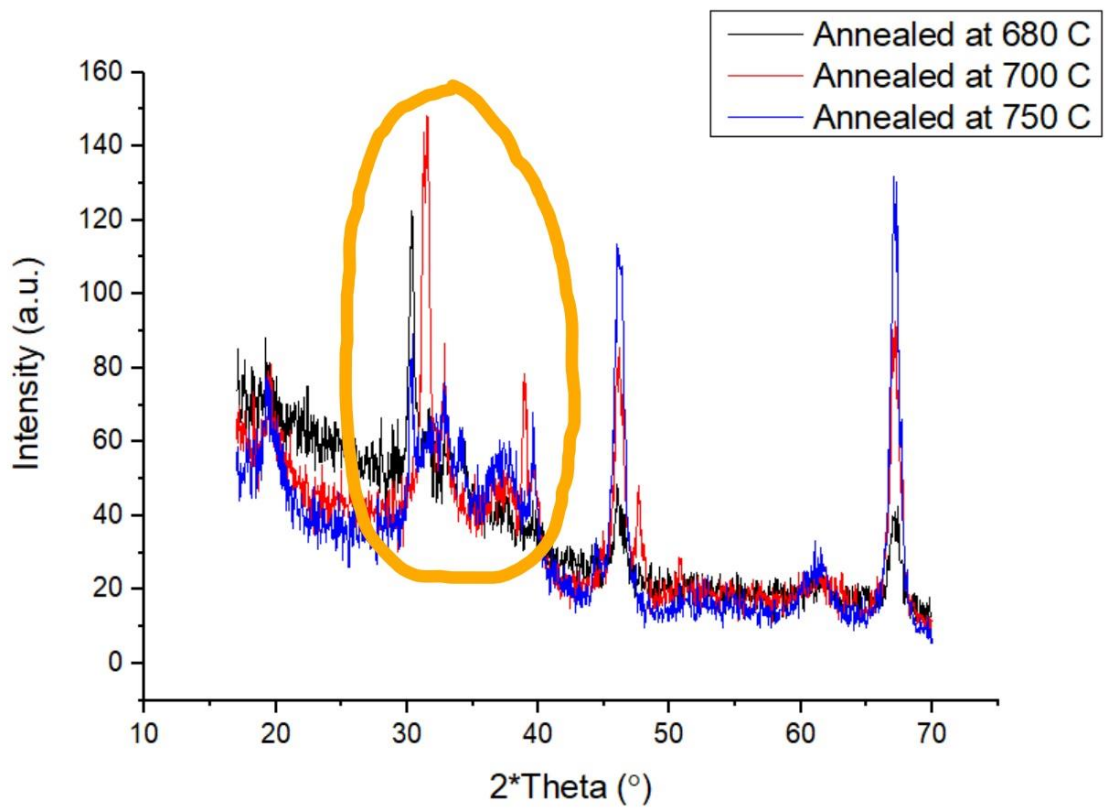


Fig. 4.19- XRD for $1\ \mu\text{m}$ sample annealed at different temperatures for 12 h.

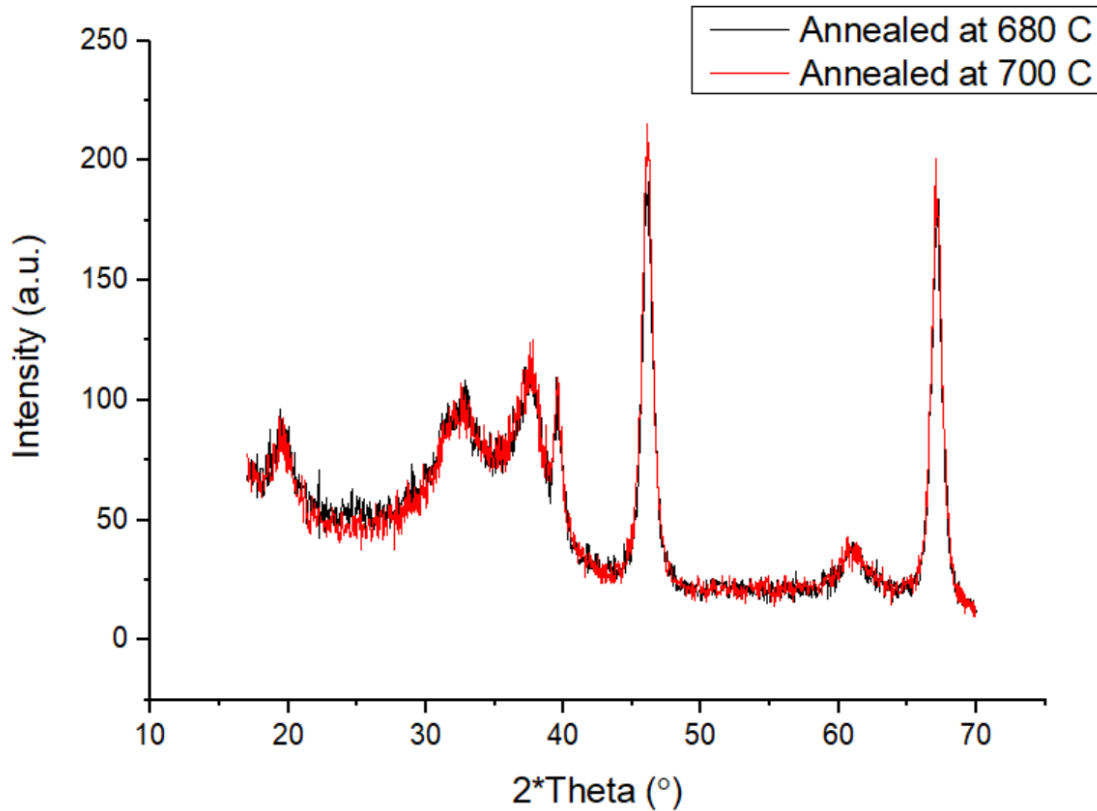


Fig. 4.20- XRD for 2 μm annealed at different temperatures for 12 h.

From those figures, the crystallization of the different thicknesses happens already at lower temperatures than 750 °C, where the peaks of γ -alumina phase start to appear, that lead us to the fact that the two annealed samples we are working on have at least gone through some minor crystallization, despite the fact that they have been annealed for only 45 and 30 minutes.

Figures 4.21 and 4.22 show XRD for our 1 μm and 2 μm annealed samples respectively, and as thought, crystallization started to occur already for the 1 μm sample even though the annealing was done for only 45 minutes, while for the 2 μm sample a crystallization is not so obvious though some microstructural changes can be noticed from the yet to grow peaks below the red lines, and the reason for the discrepancy between the two samples is the different annealing times. The peaks of the two samples coincide with the previously shown peaks of the samples annealed for 12 h at IIT.

Going through the same method used with the 2 μm and 1 μm of the as-deposit samples, utilizing Rayleigh waves and bulk longitudinal waves propagating within the films. As seen from figure 4.23, two frequency spectra of the 2 μm and 1 μm annealed samples, upper and lower respectively, taken with 50° laser incident angle, where Rayleigh wave and bulk transverse wave of silicon substrate, shown with the red and blue lines above them, respectively, are clear and intense enough. While the bulk longitudinal waves of annealed Al₂O₃ are not clear enough, though you can see them quite clearly at the anti-stokes events, shown with yellow lines.

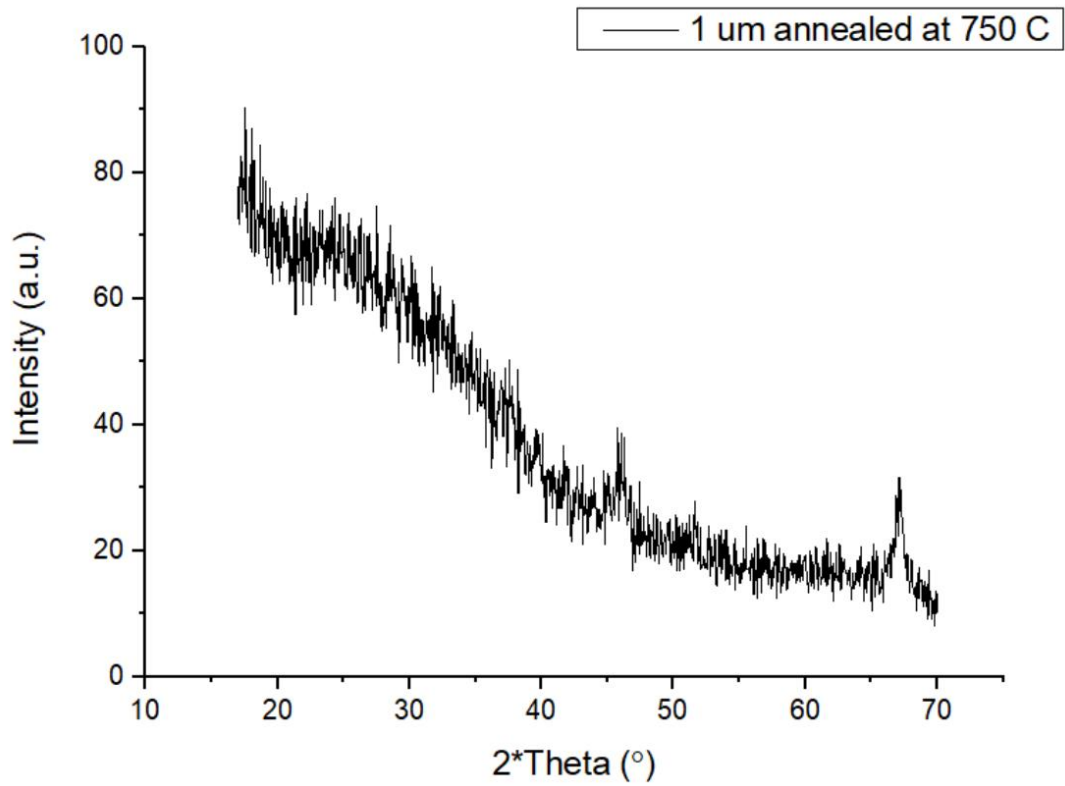


Fig. 4.21- XRD for 1 μm sample annealed at 750 $^{\circ}\text{C}$ for 45 minutes.

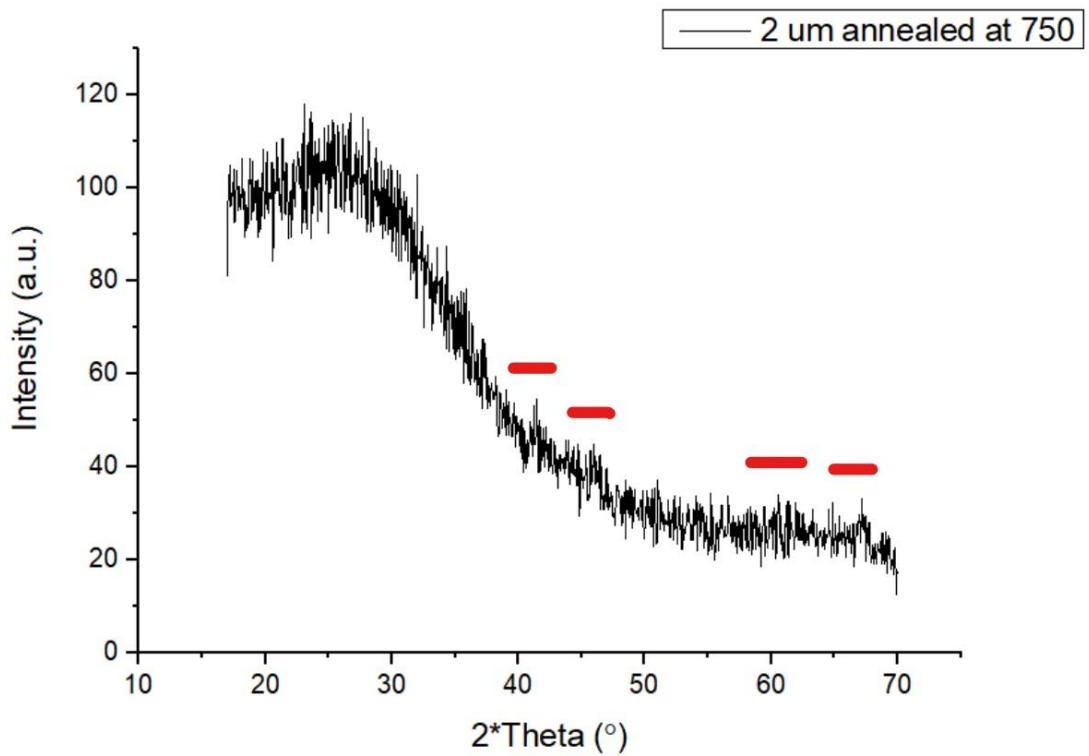


Fig. 4.22- XRD for 2 μm sample annealed at 750 $^{\circ}\text{C}$ for 30 minutes.

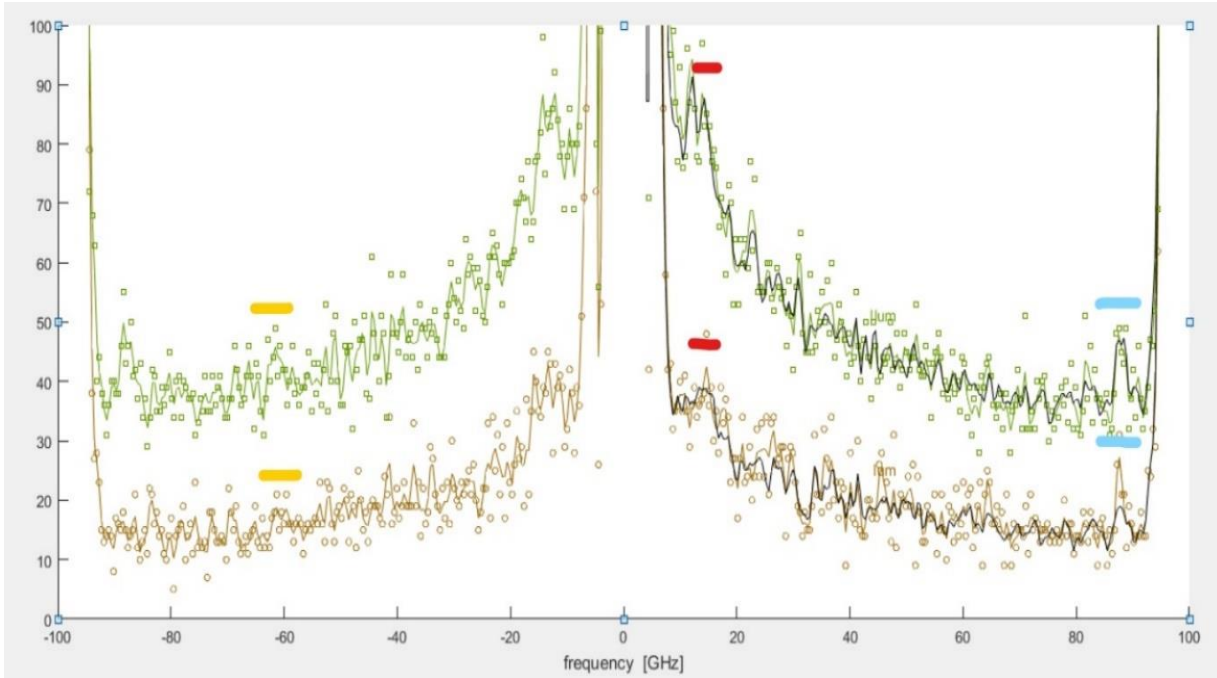


Fig 4.23- Frequency spectra of 2 μm and 1 μm annealed samples, upper and lower respectively.

We are going to rely on these spectra to get the elastic moduli of the annealed samples, although much more investigation is needed but time is not helping at all. Tables 4.6 and 4.7 show elastic moduli of the different annealed samples.

Figure 4.24 shows the difference in Young's moduli of as-deposit and annealed samples, as can be noticed the annealed samples have the higher E , but not substantially higher since the microstructural changes are not that big. Having higher E means they are more brittle, and from the microstructural point of view, the atoms are better packed and more organized.

Table 4.6

Young's modulus E , Poisson ratio ν , bulk modulus B , shear modulus G and elastic constants (C_{11} , C_{44}) values of the 1 μm annealed sample, the column on the right corresponds to the standard deviation from the mean value.

E (GPa)	227	± 5
ν	0.32	± 0.01
B (GPa)	213	± 9
G (GPa) = C_{44}	86	± 2
C_{11}	327	± 11

Table 4.7

Young's modulus E , Poisson ratio ν , bulk modulus B , shear modulus G and elastic constants (C_{11} , C_{44}) values of the $2\ \mu\text{m}$ annealed sample, the column on the right corresponds to the standard deviation from the mean value.

E (GPa)	222	± 5
ν	0.33	± 0.01
B (GPa)	216	± 9
G (GPa) = C_{44}	84	± 1
C_{11}	227	± 11

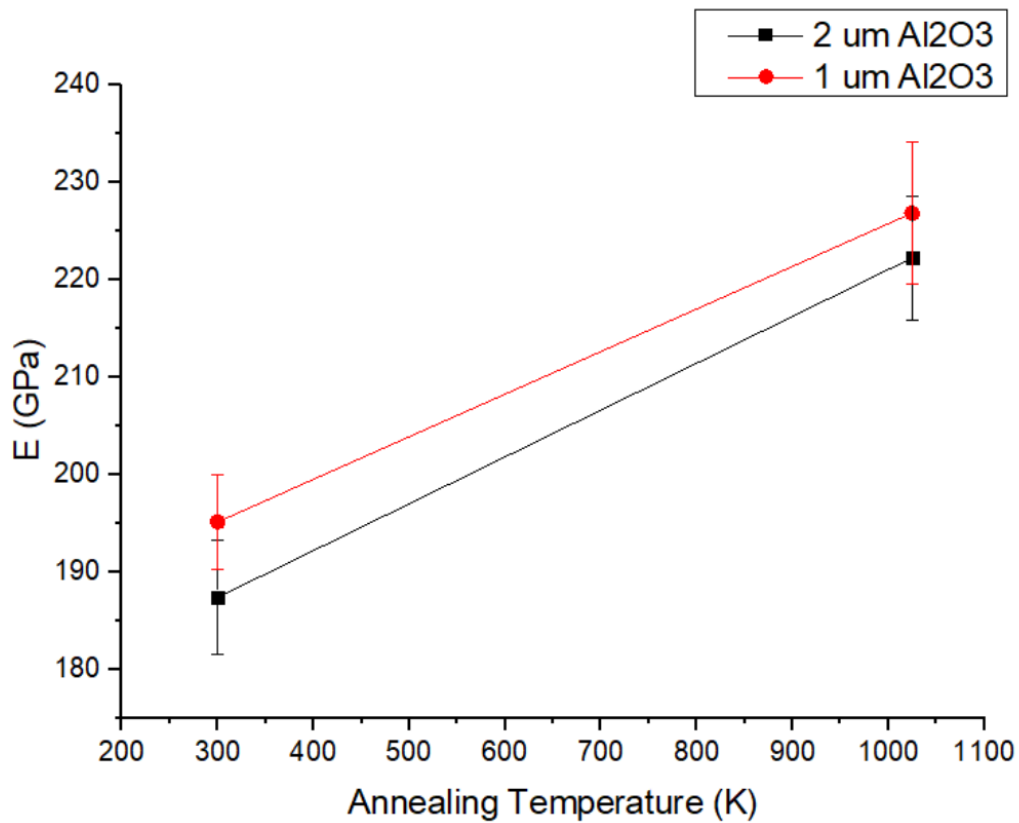


Fig. 4.24- Plot of Young's moduli of as-deposit and annealed $2\ \mu\text{m}$ and $1\ \mu\text{m}$ samples, black and red curves respectively.

4.5 Scattered Data on Y2O3

a) Residual Stresses

As in the case of alumina, again a residual stresses measurement has been done on yttria samples with different thicknesses, shown in figure 4.25. The same trend as the one observed in alumina samples can be seen from the plot, with only one difference, this time the magnitudes of the residual stresses are much lower than the one observed with alumina samples.

As a hypothesis for the reason behind this is that this time the deposition has been done on the samples while they were fixed by a double-face tape at the middle of the back of the silicon substrate, leaving the frame of the substrate free with no imposed forces on it which may have led to an increase in the residual stresses.

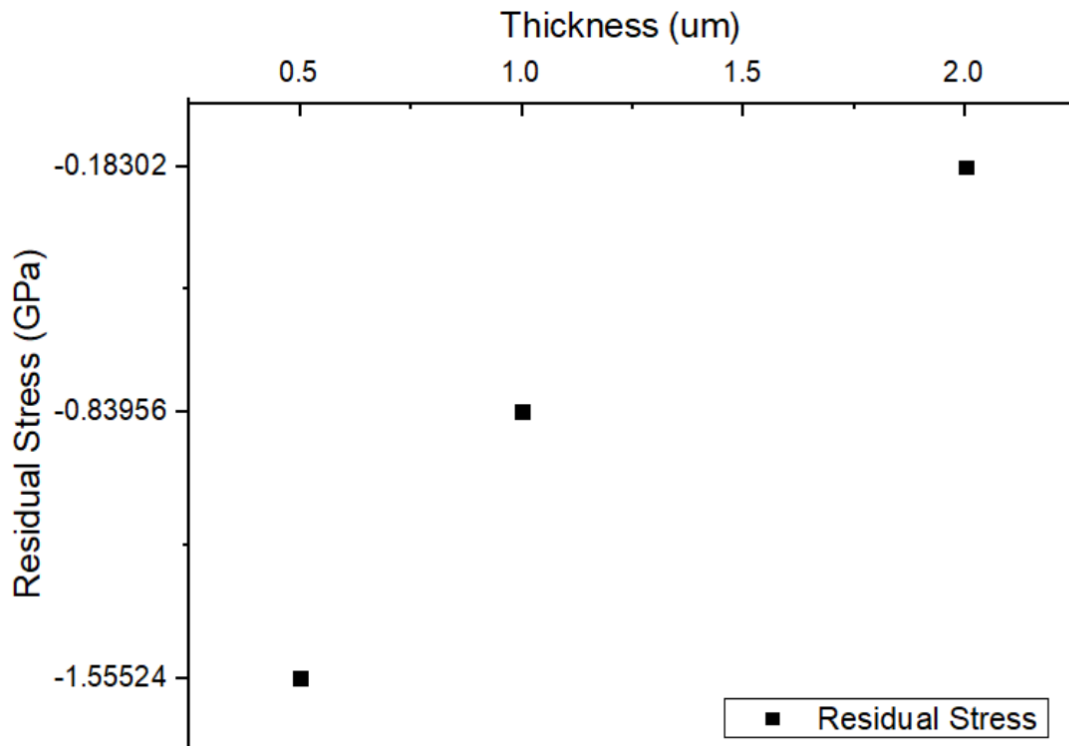


Fig. 4.25- Residual stress within Y2O3 thin films at different thicknesses.

b) Brillouin measurement

While acquiring the frequency spectra for different yttria samples, we reached the conclusion of not being interested anymore in this material for the previously mentioned reasons. So, the data analysis of yttria's different spectra was never completed, and thus, the elastic constants as well as the elastic moduli, have never been estimated.

Shown in figure 4.26, a frequency spectrum of a $1\ \mu\text{m}$ yttria film at 60° laser incident angle, again as in the case of alumina, three peaks colored with green, orange and yellow lines above each of them are Rayleigh, bulk longitudinal of the film and bulk transverse of the silicon substrate waves, respectively. Furthermore, an extra fourth peak is shown this time which is corresponding to the bulk longitudinal wave of silicon. The film is again transparent to the incident laser beam since we can observe peaks corresponding to bulk transverse and longitudinal waves of silicon.

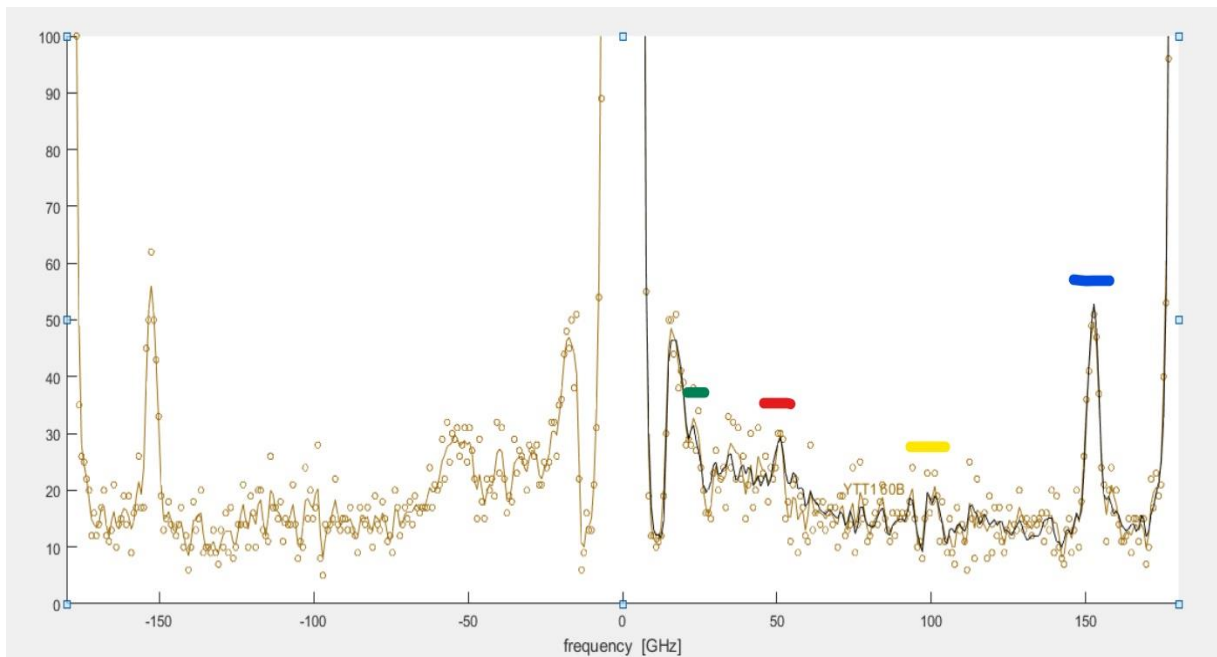


Fig. 4.26- Frequency spectrum of $1\ \mu\text{m}$ yttrium oxide coating, the peaks colored with green, red, orange and blue are Rayleigh, bulk longitudinal of yttria, bulk transverse and bulk longitudinal of silicon, respectively.

c) Behavior of Yttria Under Thermal Loads

Since we did not extract yttria's elastic moduli, CTEs of the different yttria samples are not possible to be acquired. Nevertheless, we have been able to see the evolution of the residual stresses under the temperature variation, seen in figure 4.27.

The measurement was done till ~ 275 °C and then cooling back the sample, as can be seen, a transition temperature at around 220 °C occurs which is linked to the crystallization of yttria sample, becoming more brittle than its amorphous phase. This piece of information is proved through XRD measurement, done at Istituto Italiano di Tecnologia (IIT) in Milan, as shown in figure 4.28.

The slopes of the lower and upper curves are quite different, the lower one having the higher slope, this indicates that a change in the properties has occurred, and the CTE of the amorphous phase is higher than that of the crystalline material. That goes along with what is expected since the annealed samples are expected to have higher E than that of amorphous samples.

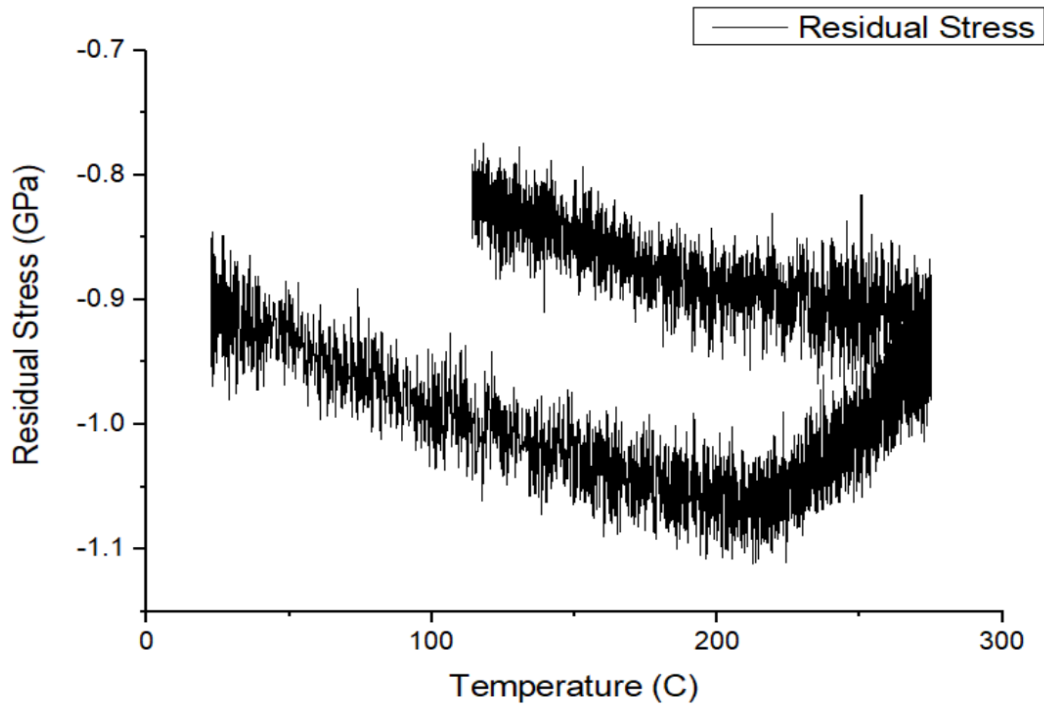


Fig. 4.27- Evolution of residual stress within yttria 1 μm film under temperature variation.

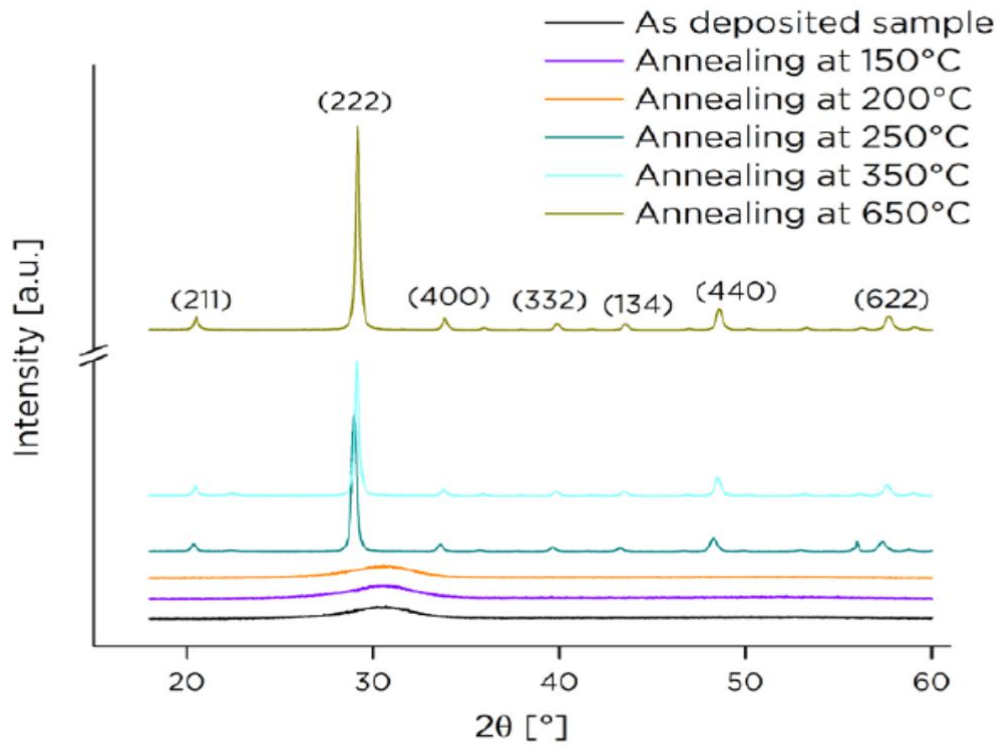


Fig. 4.28- XRD patterns for yttria film under different annealing temperature [105].

5. Conclusions and Perspectives

Coming to the last chapter of this book, conclusions of what have been done during this work is to be giving alongside some perspectives of what may have been done or what kind of investigation could be considered in the future.

5.1 Conclusions

Materials are always considered as one of the most important aspects for different technologies' developments. Furthermore, they define the efficiency, the lifespan of a plant and the economics behind any application.

Energy demand is considered one of the main issues of nowadays life where fossil fuel is still used up to now in a threatening rate, knowing their huge damage they cause to the atmosphere of earth and the climate change they cause, yet they are still used for their availability and suitability. Renewables are still in the growing phase as technology and they are not yet considered as a sustainable enough source of energy.

Nuclear energy has proven through the years their reliability and efficiency as an energy source, as well as they are considered as a green and free of CO₂ emission source. One type of nuclear reactors is lead-cooled fast neutron reactors which have some advantages over the thermal ones, like compactness, higher power density and higher Burnup. They also have some drawbacks and one of them is the severe environment (high irradiation, thermal loads and lead corrosion) the structural materials are under while the operation of the reactor.

That is the main application and the reason why throughout this book, a study of thermo-mechanical properties for different oxide coatings have been done, as they are considered as good choices for the protection of the structural materials of the fast reactors against wear and corrosion.

The task was to get the mechanical properties of the oxide coatings represented by the elastic moduli using Brillouin Spectroscopy. Also, determining the residual stresses which arise within the thin films due to the deposition process itself, alongside, the coefficient of thermal expansion, through the substrate curvature setup.

Here are the conclusions reached applying those characterization techniques:

- ❖ Residual stresses arise within deposited coatings are either of intrinsic nature, because of the deposition process itself, or of extrinsic nature as a result of a CTE mismatch between that of the film and the one of substrate.
- ❖ The residual stresses arising because of film extension are of compressive nature, having the highest compressive stress for the thinnest sample and then decreases with higher thicknesses because of the higher number of defects that is expected with higher thicknesses, which leads to some sort of relaxation process. That may lead eventually and at some thickness point to reach a tensile state of stress within the film after passing through a zero stresses point.
- ❖ The way samples are fixed to the holder while depositing the film may affect the magnitude of the created residual stresses significantly, so a sample which is under some imposed forces along its frame will accommodate higher stresses than the one left free.

- ❖ Elastic moduli of the different thicknesses showed no big differences in the magnitudes, and this was expected since all the samples were deposited under the same conditions.
- ❖ Behavior of aluminum oxide under thermal loads showed good thermodynamic stability as there are no phase transitions or any sign of crystallization at least up to 600 C.
- ❖ CTE calculations showed a consistent trend with that of Young's modulus with respect to the thickness, where they are higher for samples where E are lower and vice versa.
- ❖ Elastic moduli of the two 750 °C annealed alumina samples have been acquired, as expected, they showed slightly higher Young's moduli than that of as-deposit alumina samples, which means they became a bit more brittle and stiffer.
- ❖ XRD patterns for the annealing process of alumina suggest that there is a correlation between the crystallization temperature and the thickness of the sample, where at lower thicknesses, higher thermal energy is required to introduce the crystallization phase, and it is thought that this is related to the size of the bulk volume, though deeper investigation is needed to confirm this hypothesis.
- ❖ Trying to investigate yttria samples showed us a transition temperature where a crystallization happens at around 220 C, but then it stabilizes till the melting point of the material. Crystallization at that low temperature means that the material starts losing its appealing properties early, that is mainly why we stopped the characterization procedures for that material.
- ❖ Residual stresses measurements for yttria showed a similar trend of that of alumina which proves the theory mentioned above, furthermore, the lower magnitudes of residual stresses in this case is because of the way this material was fixed during deposition as previously stated.

In conclusion, aluminum oxide coatings grown by PLD have shown good mechanical properties, especially the ones grown with lower thicknesses since they show the same elastic moduli as the ones with higher thicknesses. They also have higher compressive residual stresses that allow them to accommodate higher tensile stresses during operation, furthermore, they start crystallizing at higher temperature than the thicker samples, which means their amorphous phase is more stable. All these features make of PLD grown alumina with thin thickness a good candidate as a protective coating for the cladding.

5.2 Perspectives & Future Outlooks

Coming to the final part of this thesis work, it is quite important to mention the things that had to be made, or that which would have made the work a bit more efficient, alongside what may be further considered in the future, just in case of any interests to conduct a similar study.

- ❖ Mechanical and thermal characterization of different oxide coatings under different deposition techniques and at different conditions may be conducted just to correlate between the different deposition parameters and thermo-mechanical properties of the coatings.
- ❖ More investigations are needed for the annealed alumina samples to prove/disprove the current results of elastic moduli.
- ❖ Deepen the study of the intrinsic residual stresses, which and link it with the conditions under which the deposition occurred, to finally reach a way of engineering coatings with the desired residual stresses according to the application used.
- ❖ Nano-indentation measurements may be done in order to facilitate the data analysis of Brillouin measurements, and it will also help with results verification alongside getting information about the hardness of the coating's surface.
- ❖ Tests to assess corrosion resistance of the different coatings may be considered under stagnant and flowing lead, to be able to observe the chemical and structural effects of such process.
- ❖ Investigating thermo-mechanical properties for irradiated coatings under different displacement per atom (dpa), alongside, observing structural and morphological changes within the coatings and see if any sort of phase transitions occurs.

Coming to an end of this thesis book, I would like to conclude it by stating that Al_2O_3 is a worth investigating material for the interesting properties it has, and any other oxide which may hold some common features with alumina should also be studied.

Acknowledgments

I thank anyone helped or participated in making this work the way it is. I thank all the PhD students working in the Nano-lab of Politecnico di Milano, Andrea Pazzaglia for helping with LabVIEW codes, Beatrice Bricchi, Michele Sala and Sonia Peggiani for their help whenever I had any need.

I would like to extend my thanks to Edoardo Besozzi for providing me with huge help, especially with the CTE measurements and how to conduct them, also thanks to Davide Dellasega for helping me with SEM measurements.

Thanks to the members of the PLD group (Istituto Italiano di Tecnologia, Milan) for providing me with the different samples of both, yttria and alumina. Special thanks to Dr. Fabio di Fonzo and Matteo Vanazzi for their patience, their continuous help and for providing me with the right steps to go through this work. Thanks to Boris Paladino for providing help whenever it was needed.

Above all I thank Prof. Marco Beghi (department of Energy, Politecnico di Milano), who guided me the whole time, for teaching me how to use Brillouin Spectroscopy, which is not easy, and for his continuous help through this work and for his priceless advises.

Special thanks to my family for supporting me through all my life and for giving me the strength and courage to be the guy I am now. Thanks to my friends for always being there for me.

Finally, thank you, Magdalena, for encouraging me and for being by my side all the time.

Essam Serag

References

- [1] G.D. Wilk, R.M. Wallace, J.M. Anthony, High- κ gate dielectrics: Current status and materials properties considerations, *J. Appl. Phys.* 89 (2001) 5243.
- [2] J. Niinistö, M. Putkonen, L. Niinistö, Processing of Y₂O₃ Thin Films by Atomic Layer Deposition from Cyclopentadienyl-Type Compounds and Water as Precursors, *Chem. Mater.* 16 (2004) 2953.
- [3] J. Kwo, M. Hong, A.R. Kortan, K.T. Queeney, Y.J. Chabal, J.P. Mannaerts, T. Boone, J.J. Krajewski, A.M. Sergent, J.M. Rosamilla, High ϵ gate dielectrics Gd₂O₃ and Y₂O₃ for silicon *Appl. Phys. Lett.* 77 (2000) 130.
- [4] F. Paumier, R.J. Gaboriaud, A. Kaul, Yttrium oxide thin films: chemistry-stoichiometry-strain and microstructure, *Cryst. Eng.* 5 (2002) 169.
- [5] P. de Rouffignac, J.-S. Park, R.G. Gordon, Atomic Layer Deposition of Y₂O₃ Thin Films from Yttrium Tris(N,N'-diisopropylacetamidinate) and Water, *Chem. Mater.* 17 (2005) 4808.
- [6] W.O. Gordon, B.M. Tissue, J.R. Morris, Adsorption and Decomposition of Dimethyl Methylphosphonate on Y₂O₃ Nanoparticles, *J. Phys. Chem. C* 111 (2007) 3233.
- [7] S. Zhang, R. Xiao, Yttrium oxide films prepared by pulsed laser deposition, *J. Appl. Phys.* 83 (1998) 3842.
- [8] Y. Zhao, K. Kita, K. Kyuno, A. Toriumi, Band gap enhancement and electrical properties of La₂O₃ films doped with Y₂O₃ as high-k gate insulators, *Appl. Phys. Lett.* 94 (2009) 042901.
- [9] A.C. Rastogi, R.N. Sharma, Interfacial charge trapping in extrinsic Y₂O₃/SiO₂ bilayer gate dielectric-based MIS devices on Si (100), *Semicond. Sci. Technol.* 16 (2001) 641.
- [10] J.Y. Cho, K.-Y. Ko, Y.R. Do, Optical properties of sol-gel derived Y₂O₃: Eu³⁺ thin-film phosphors for display applications, *Thin Solid Films* 515 (2007) 3373.
- [11] W.M. Lau, Use of surface charging in x-ray photoelectron spectroscopic studies of ultrathin dielectric films on semiconductors, *Appl. Phys. Lett.* 54 (1989) 338.
- [12] S.Y. Chiam, W.K. Chim, C. Pi, A.C.H. Huan, S.J. Wang, J.S. Pan, S. Turner, J. Zhang, Band alignment of yttrium oxide on various relaxed and strained semiconductor substrates, *J. Appl. Phys.* 103 (2008) 083702.

- [13] C. Cannas, M. Casu, M. Mainas, A. Musinu, G. Piccaluga, S. Polizzi, A. Speghini, M. Bettinelli, Synthesis, characterisation and optical properties of nanocrystalline Y₂O₃:Eu³⁺ dispersed in a silica matrix by a deposition–precipitation method, *J. Mater. Chem.* 13 (2003) 3079.
- [14] S. Ekambaram, K.C. Patil, M. Maaza, Synthesis of lamp phosphors: facile combustion approach, *J. Alloys Compd.* 393 (2005) 81.
- [15] B. Mercier, C. Dujardin, G. Ledoux, C. Louis, O. Tillement, P. Perriat, Observation of the gap blueshift on Gd₂O₃:Eu³⁺ nanoparticles *J. Appl. Phys.* 96 (2004) 650.
- [16] T.H. Hsu, H.C. You, F.H. Ko, T.F. Lei, PolySi-SiO₂-ZrO₂-SiO₂-Si flash memory incorporating a sol-gel-derived ZrO₂ charge trapping layer, *J. Electrochem. Soc.* 153 (2006) G934.
- [17] T.M. Pan, J.W. Chen, *Appl. Phys. Lett.* 23 (2008) 183510.
- [18] Y.N. Tan, W.K. Chim, B.J. Cho, W.K. Choi, Over-erase phenomenon in SONOS-type flash memory and its minimization using a hafnium oxide charge storage layer, *IEEE Trans. Electron. Dev.* 51 (2004) 1143.
- [19] R.J. Gaboriaud, F. Pailloux, P. Guerin, F. Paumier, Yttrium sesquioxide, Y₂O₃, thin films deposited on Si by ion beam sputtering: microstructure and dielectric properties, *Thin Solid Films* 400 (2001) 106.
- [20] T. Minami, M. Yamazaki, T. Miyata, Y. Kobayashi, T. Shirai, A new thin-film phosphor using multicomponent oxides composed of Y₂O₃ and GeO₂, *Thin Solid Films* 411 (2002) 161.
- [21] C.V. Ramana, V.H. Mudavakkat, K. Kamala Bharathi, V.V. Atuchin, L.D. Pokrovsky, V.N. Kruchinin, Enhanced optical constants of nanocrystalline yttrium oxide thin films, *Appl. Phys. Lett.* 98 (2011) 031905.
- [22] V.H. Mudavakkat, M. Noor-A-Alam, K. Kamala Bharathi, S. AlFaify, A. Dissanayake, A. Kayani, C.V. Ramana, Structure and AC conductivity of nanocrystalline Yttrium oxide thin films, *Thin Solid Films* 519 (2011) 7947.
- [23] B. Lacroix, F. Paumier, R.J. Gaboriad, Crystal defects and related stress in Y₂O₃ thin films: Origin, modeling, and consequence on the stability of the C-type structure, *Phys. Rev. B* 84 (2011) 014104.
- [24] V. Swamy, N.A. Dubrovinskaya, L.S. Dubrovinsky, High-temperature powder x-ray diffraction of yttria to melting point, *J. Mater. Res.* 14 (1999) 456.
- [25] B.H. O'Connor, T.M. Valentine, A neutron diffraction study of the crystal structure of the C-form of yttrium sesquioxide, *Acta Crystallogr. B* 25 (1969) 2140.

- [26] L. Lou, W. Zhang, A. Brioude, C. Le Luyer, J. Mugnier, Preparation and characterization of sol-gel Y₂O₃ planar waveguides, *Opt. Mater.* 18 (2001) 331.
- [27] J.H. Shim, C.-C. Chao, H. Huang, F.B. Prinz, Atomic layer deposition of yttria-stabilized zirconia for solid oxide fuel cells, *Chem. Mater.* 19 (2007) 3850.
- [28] H. Huang, M. Nakamura, P. Su, R. Fasching, Y. Saito, F.B. Prinz, High-performance ultrathin solid oxide fuel cells for low-temperature operation, *J. Electrochem. Soc.* 154 (2007) B20.
- [29] L.M. Wang, S. Zhu, R.C. Ewing, U.S. Department Of Energy's nuclear engineering education research: highlights of recent and current research-III. 1. Behavior of Fission Products in YSZ-Based Inert Matrix Fuel, *T. Am. Nucl. Soc.* 84 (2001) 103.
- [30] S. Zhu, X.T. Zu, L.M. Wang, R.C. Ewing, Nanodomains of pyrochlore formed by Ti ion implantation in yttria-stabilized zirconia, *Appl. Phys. Lett.* 80 (2002) 4327.
- [31] S. Zhu, X.T. Zu, L.M. Wang, R.C. Ewing, Cesium Ion Implantation in Single Crystal Yttria-Stabilized Zirconia (YSZ) and Polycrystalline MgAl₂O₄-YSZ, *Mater. Res. Soc. Proc.* 713 (2002) JJ11.
- [32] X. Xiang, X.T. Zu, S. Zhu, C.F. Zhang, Z.G. Wang, L.M. Wang, R.C. Ewing, XPS and optical studies of Xe⁺-implanted and annealed YSZ single crystals, *Nucl. Instrum. Methods* 250 (2006) 382.
- [33] W.L. Lu, L. Xiao, D. Xu, J.N. Qin, D. Zhang, Microstructural characterization of Y₂O₃ in in situ synthesized titanium matrix composites, *J. Alloys Compd.* 433 (2007) 140.
- [34] B.J. Gibbons, M.E. Hawley, S. Trolrier-McKinstry, D.G. Schlom, Real-time spectroscopic ellipsometry as a characterization tool for oxide molecular beam epitaxy, *J. Vac. Sci. Technol. A* 19 (2001) 584.
- [35] J.C. Vyas, G.P. Kothiyal, K.P. Muthe, D.P. Gandhi, A.K. Debnath, S.C. Sabharwal, M.K. Gupta, Growth of yttria and dysprosium thin films by molecular beam epitaxy and their characterization, *J. Cryst. Growth* 130 (1993) 59.
- [36] H. Fukumoto, T. Imura, Y. Osaka, Heteroepitaxial growth of Y₂O₃ films on silicon, *Appl. Phys. Lett.* 55 (1989) 360.
- [37] R.N. Sharma, T. Lakshmi, R.C. Rastogi, Large-eddy simulation of the convective boundary layer-A comparison of four computer codes, *Thin Solid Films* 1 (1991) 1.
- [38] J.H. Gao, D. Kumar, K.G. Cho, P.H. Holloway, R.K. Singh, X.D. Fan, Y. Yan, S.J. Pennycook, Epitaxial growth of Y₂O₃:Eu thin films on LaAlO₃, *Appl. Phys. Lett.* 75 (1999) 2223.

- [39] S.L. Jones, D. Kumar, R.K. Singh, P.H. Holloway, Luminescence of pulsed laser deposited Eu doped yttrium oxide films, *Appl. Phys. Lett.* 71 (1997) 404.
- [40] S. Zhang, R. Xiang, Yttrium oxide films prepared by pulsed laser deposition, *J. Appl. Phys.* 83 (1998) 3842.
- [41] M.B. Korzenski, P.H. Lecoer, B. Mercey, D. Chippaux, B. Raveau, R. Desfeux, PLD-Grown Y2O3 Thin Films from Y Metal: An Advantageous Alternative to Films Deposited from Yttria, *Chem. Mater.* 12 (2000) 3139.
- [42] Q. Hou, Z. Huang, J. Gao, Effects of Y2O3 on the microstructure and wear resistance of cobalt-based alloy coatings deposited by plasma transferred arc process, *Rare Met.* 26 (2007) 103.
- [43] H.-S. Kim, C. Park, R.-K. Ko, D. Shi, J.-K. Chung, H.-S. Ha, Y.-M. Park, K.-J. Song, D.-J. Youm, High rate DC-reactive sputter deposition of Y2O3 film on the textured metal substrate for the superconducting coated conductor, *Physica C* 426 (2005) 926.
- [44] H. Horng, D.S. Wu, J.W. Yu, C.Y. Kung, Effects of rapid thermal process on structural and electrical characteristics of Y2O3 thin films by rf-magnetron sputtering, *Thin Solid Films* 289 (1996) 234.
- [45] E.K. Evangelou, C. Wiemer, M. Fanciulli, M. Sethu, W. Cranton, Electrical and structural characteristics of yttrium oxide films deposited by rf-magnetron sputtering on n-Si, *J. Appl. Phys.* 94 (2003) 318.
- [46] V.V. Bakovets, T.M. Levashova, V.T. Ratushnyak, L.F. Bakhturova, Chemical Vapor Deposition of Y2O3 Films Using Y(dpm)3, *Inorg. Mater.* 38 (2002) 371.
- [47] J. Selvakumar, V.S. Raghunathan, K.S. Nagaraja, Nanocrystalline yttria films by plasma-assisted liquid injection (PA-LI) CVD technique using metallorganic precursors, *Mater. Lett.* 63 (2009) 2710.
- [48] D. Niu, R.W. Ashcraft, Z. Chen, S. Stemmer, G.N. Parsons, Chemical, physical, and electrical characterizations of oxygen plasma assisted chemical vapor deposited yttrium oxide on silicon, *J. Electrochem. Soc.* 150 (2003) F102.
- [49] S.A. Barve, N. Jagannath, Mithal, M.N. Deo, N. Chand, B.M. Bhanage, L.M. Gantayet, D.S. Patil, Microwave ECR plasma CVD of cubic Y2O3 coatings and their characterization, *Surf. Coat. Technol.* 204 (2010) 3167.
- [50] T. Gougousi, Z. Chen, Deposition of yttrium oxide thin films in supercritical carbon dioxide, *Thin Solid Films* 516 (2008) 6197.
- [51] W.H. Chang, P. Chang, W.C. Lee, T.Y. Lai, J. Kwo, C.H. Hsu, J.M. Hong, M. Hong, Epitaxial stabilization of a monoclinic phase in Y2O3 films on c-plane GaN, *J. Cryst. Growth* 323 (2011) 107–110.

- [52] R.J. Gaboriaud, F. Paumier, M. Jublot, B. Lacroix, Ion irradiation-induced phase transformation mechanisms in Y2O3 thin films, *Nucl. Instrum. Methods in Phys. Res. Sect. B* 311 (2013) 86–92.
- [53] M. Zinkevich, Thermodynamics of rare earth sesquioxides, *Prog. Mater. Sci.* 52 (2007) 597–647.
- [54] D.Djurovic, M. Zinkevich, F. Aldinger, Thermodynamic modeling of the yttrium–oxygen system, *Calphad* 31 (2007) 560–566.
- [55] R.J. Gaboriaud, M. Jublot, F. Paumier, B. Lacroix, Phase transformations in Y2O3 thin films under swift Xe ions irradiation, *Nucl. Instrum. Methods Phys. Res., Sect. B* 310 (2013) 6–9.
- [56] R.J. Gaboriaud, F. Paumier, F. Pailloux, P. Guerin, Y2O3 thin films: internal stress and microstructure, *Mater. Sci. Eng., B* 109 (1-3) (2004) 34–38.
- [57] D.B. Chrisey, G.K. Hubler (Eds.), *Pulsed Laser Deposition of Thin Films*, Wiley Interscience, New York, 1994.
- [58] Michael N.R. Ashfold, Frederick Claeysens, Gareth M. Fuge, Simon J. Henley, Pulsed laser ablation and deposition of thin films, *Chem. Soc. Rev.* 33 (2004) 23–31.
- [59] Sucharita Sinha, T.R.G. Kutty, P.V.A. Padmanabhan, K.G.K. Warriar, J. Laser Appl., Pulsed laser deposition of lanthanum phosphate protective films, 21 (3) (2009) 149–153.
- [60] P.R. Willmott, J.R. Huber, Pulsed laser vaporization and deposition, *Rev. Mod. Phys.* 72 (1) (2000) 315–328.
- [61] T.J. Jackson, S B Palmer, Oxide superconductor and magnetic metal thin film deposition by pulsed laser ablation: a review, *J. Phys. D: Appl. Phys.* 27 (1994) 1581–1594.
- [62] J. Greer, Large-area commercial pulsed laser deposition, in: R. Eason (Ed.), *Pulsed Laser Deposition of Thin Films: Applications-Led Growth of Functional Materials*, Wiley Interscience, New York, 2007, pp. 281–304.
- [63] Balakrishnan G, Kuppusami P, Tripura Sundari S, Thirumurugesan R, Ganesan V, Mohandas E, et al., Photomechanical ablation of 304L stainless steel, aluminum oxide (Al2O3) thin film, and pure silicon, *Thin Solid Films* 2010;518:3898–902.
- [64] Gottmann J, Kreutz EW., Pulsed laser deposition of alumina and zirconia thin films on polymers and glass as optical and protective coatings, *Surf Coat Technol* 1999;116–119: 1189–94.

- [65] Cibert C, Hidalgo H, Champeaux C, Tristant P, Tristier T, Desmaison J, et al., Properties of aluminum oxide thin films deposited by pulsed laser deposition and plasma enhanced chemical vapor deposition, *Thin Solid Films* 2008;516:1290–6.
- [66] Zabinski JS, Hu JJ, Bultman JE, Pierce NA, Voevodin AA., Structural and phase changes of iron substrate upon pulse laser deposition of MoSex solid lubricating coatings, *Thin Solid Films* 2008;516:6215–9.
- [67] Adams TM, Duncan AJ, Fitz-Gerald J., Characterization of environmental stability of pulsed laser deposited oxide ceramic coatings, *J Electron Mater* (2005).
- [68] F. Di Fonzo, D. Tonini, A. Li Bassi, C.S. Casari, M.G. Beghi, C.E. Bottani, D. Gastaldi, P. Vena, R. Contro, Growth regimes in pulsed laser deposition of aluminum oxide films, *Appl. Phys. A* 93 (2008) 765–769.
- [69] F. García Ferré, E. Bertarelli, A. Chiodoni, D. Carnelli, D. Gastaldi, P. Vena, M.G. Beghi, F. Di Fonzo, The mechanical properties of a nanocrystalline Al₂O₃/a-Al₂O₃ composite coating measured by nanoindentation and Brillouin spectroscopy, *Acta Mater.* 61 (2013) 2662–2670.
- [70] J. Zhang, A review of steel corrosion by liquid lead and lead–bismuth, *Corros. Sci.* 51 (2009) 1207–1227.
- [71] I.V. Gorynin, G.P. Karzov, V.G. Markov, V.S. Lavrukhin, V.A. Yakovlev, Structural materials for atomic reactors with liquid metal heat-transfer agents in the form of lead or lead–Bismuth alloy, *Met. Sci. Heat Treat.* 41 (1999) 384–388.
- [72] X. Chen, Q. Yuan, B. Madigan, W. Xue, Long-term corrosion behavior of martensitic steel welds in static molten Pb–17Li alloy at 550 C, *Corros. Sci.* 96 (2015) 178–185.
- [73] J. Wang, S. Lu, L. Rong, D. Li, Y. Li, Effect of silicon on the oxidation resistance of 9 wt.% Cr heat resistance steels in 550° C lead-bismuth eutectic, *Corros. Sci.* 111 (2016) 13–25.
- [74] L.F. Martinelli Balbaud-Célérier, A. Terlain, S. Delpech, G. Santarini, J. Favergeon, G. Moulin, M. Tabarant, G. Picard, Oxidation mechanism of a Fe–9Cr–1Mo steel by liquid Pb–Bi eutectic alloy (Part I), *Corros. Sci.* 50 (2008) 2523–2536.
- [75] P. Hosemann, R. Dickerson, P. Dickerson, N. Li, S.A. Maloy, Transmission electron microscopy (TEM) on oxide layers formed on D9 stainless steel in lead bismuth eutectic (LBE), *Corros. Sci.* 66 (2013) 196–202.

- [76] G. Müller, A. Heinzl, J. Konys, G. Schumacher, A. Weisenburger, F. Zimmermann, V. Engelko, A. Rusanov, V. Markov, Behavior of steels in flowing liquid PbBi eutectic alloy at 420–600 C after 4000–7200 h, *J. Nucl. Mater.* 335 (2004) 163–168.
- [77] C. Shroer, O. Wedemeyer, J. Novotny, A. Skrypnik, J. Konys, Selective leaching of nickel and chromium from Type 316 austenitic steel in oxygen-containing lead–bismuth eutectic (LBE), *Corros. Sci.* (2014) 113–124.
- [78] E. Yamaki, K. Ginestar, L. Martinelli, Dissolution mechanism of 316L in lead–bismuth eutectic at 500° C, *Corros. Sci.* 53 (2011) 3075–3085.
- [79] M. Kondo, M. Takahashi, T. Suzuki, K. Ishikawa, K. Hata, S.Z. Qiu, H. Sekimoto, Metallurgical study on erosion and corrosion behaviors of steels exposed to liquid lead–bismuth flow, *J. Nucl. Mater.* 343 (2005) 349–359.
- [80] M. Del Giacco, A. Weisenburger, G. Müller, Fretting corrosion of steels for lead alloys cooled ADS, *J. Nucl. Mater.* 450 (2014) 225–236.
- [81] J. Van den Bosch, G. Coen, P. Hosemann, S.A. Maloy, On the LME susceptibility of Si enriched steels, *J. Nucl. Mater.* 429 (2012) 105–112.
- [82] X. Gong, P. Marmy, A. Volodin, B. Amin-Ahmadi, L. Qin, D. Schryvers, S. Gavrilov, E. Stergar, B. Verlinden, M. Wevers, M. Seefeldt, Multiscale investigation of quasi-brittle fracture characteristics in a 9Cr–1Mo ferritic–martensitic steel embrittled by liquid lead–bismuth under low cycle fatigue, *Corros. Sci.* 102 (2016) 137–152.
- [83] A. Jianu, G. Müller, A. Weisenburger, C. Fazio, V.G. Markov, A.D. Kashtanov, Creep-to-rupture tests of T91 steel in flowing Pb–Bi eutectic melt at 550 C, *J. Nucl. Mater.* 394 (2009) 102–108.
- [84] G. Stoney, The Tension of Metallic Films Deposited by Electrolysis, *Proceedings of the Royal Society of London. Series A, Containing Papers of a Mathematical and Physical Character* 82, no. 553 (1909), 172-75.
- [85] G.C.A.M. Janssen et al., Celebrating the 100th anniversary of the Stoney equation for film stress: Developments from polycrystalline steel strips to single crystal silicon wafers, *Thin Solid Films* 517 (2009) 1858-1867.
- [86] S.J. Zinkle, G.S. Was, Materials challenges in nuclear energy, *Acta Mater.* 61 (2013) 735–758.
- [87] Stan Grainger, Jane Blunt, *Engineering Coatings – Design and Application*, 2ed edition, Introduction chapter, Woodhead Publishing (1998).

- [88] Tsiklauri, Georgi; Talbert, Robert; Schmitt, Bruce; Filippov, Gennady; Bogoyavlensky, Roald; Grishanin, Supercritical steam cycle for nuclear power plant, Nuclear Engineering and Design, Evgenei (2005).
- [89] G. F. Matthews, Material migration in divertor Tokamaks, J. Nucl. Mater 337-339 (2005) 1-9.
- [90] J. Roth et al., Recent analysis of key plasma wall interactions issues for ITER, Journal of Nuclear Materials 390–391 (2009) 1–9.
- [91] O.K. Chopra, D.L. Smith, P.F. Tortorelli, J.H. DeVan, D.K. Sze, Fus. Tech, (1985).
- [92] P.F. Tortorelli, Dissolution kinetics of steels exposed in lead-lithium and lithium environments, J. Nucl. Mater., 191–194 (1992).
- [93] P. Hubberstey, Pb-17Li and lithium: A thermodynamic rationalisation of their radically different chemistry J. Nucl. Mater., 247 (1997).
- [94] P. Hubberstey, T. Sample, A. Terlain, The stability of tritium permeation barriers and the self-healing capability of aluminide coatings in liquid Pb-17Li, Fus. Technol., 28 (1995).
- [95] J. Konys, A. Aiello, G. Benamati, L. Giancarli, Status of tritium permeation barrier development in the EU, Fus. Sci. Technol., 47 (2005).
- [96] Tribikram Kundu, Marco G. Beghi, Arthur G. Every, Pavel V. Zinin, ULTRASONIC NONDESTRUCTIVE EVALUATION, Brillouin Scattering Measurement of SAW Velocities for Determining Near-Surface Elastic Properties, CRC Press (2004).
- [97] Elena R. Dobrovinskaya, Leonid A. Lytvynov, Valerian Pishchik, Sapphire, Properties of Sapphire, Springer Science & Business Media, LLC 2009.
- [98] B.A.Pint, K.L.More, Transformation of Al₂O₃ to LiAlO₂ in Pb-17Li at 800 °C, Journal of Nuc. Mater., Elsevier (2007).
- [99] Timothy C. May-Smith, Katherine A. Sloyan, Rossana Gazia, and Robert W. Eason, Stress Engineering and Optimization of Thick Garnet Crystal Films Grown by Pulsed Laser Deposition, Crystal Growth and Design, Optoelectronics Research Centre, University of Southampton, Highfield, Southampton SO17 1BJ, U.K.
- [100] J H.C. Stumpf, A.S. Russel, J.W. Newsome and C.M. Tucker, indo Eng. Chem., 42 (7) (1950) 1398.
- [101] J L. Pauling and S.B. Hendricks, J. Am. Chem. Soc; 47 (1925) 781.

- [102] J R.E. Newnham and Y.M. de Hahn, *Z. Kristallogr.*, 117 (1962) 235.
- [103] J M.L. Kronberg, *Acta Metall.*, 5 (1957) 507.
- [104] J I. Skogsmo, P. Liu, C. Chatfield and H. Norden, in H. Bildstein and H.M. Ortner (eds.), *Proc. 12th Int. Plansee Seminar, Vol. 3, Metallwerk Plansee, Reutte, Austria, 1989*, pp. 129-142.
- [105] Boris Paladino, *Design of a Multifunctional Yttrium Oxide Coating for Breeding Blanket Concepts*, Thesis Work at Politecnico di Milano (2017).